HOKKAIDO UNIVERSITY

Title	Development of F82H-based composite materials with a high thermal conductivity
Author(s)	Heo, Jeongwoo
Degree Grantor	北海道大学
Degree Name	博士(工学)
Dissertation Number	甲第14871号
Issue Date	2022-03-24
DOI	https://doi.org/10.14943/doctoral.k14871
Doc URL	https://hdl.handle.net/2115/88691
Type	doctoral thesis
File Information	Heo_Jeongwoo.pdf

Hokkaido University Collection of Scholarly and Academic Papers : HUSCAP

Development of F82H-based composite materials with a high thermal conductivity

HOKKAIDO UNIVERSITY

Jeongwoo Heo

Graduate School of Engineering

Hokkaido University

Abstract

If a nuclear fusion reactor is developed, it can stably obtain electrical energy greater than that of existing nuclear power plants, even in the face of external shocks such as natural disasters. For this reason, research on the development of structural materials for fusion reactors is currently underway in advanced countries. In particular, reduced activation ferritic martensitic (RAFM) steel is mentioned as one of the strong candidates for fusion reactor structural materials due to its low coefficient of thermal expansion, stress corrosion cracking resistance, swelling resistance, and He brittleness resistance. However, common issues to be solved can be divided into two main issues. One is the material hardening/brittleness problem that occurs under high-energy neutron irradiation, and the other is that it is difficult to transfer the heat load to the cooling pipe quickly due to the low thermal conductivity.

In this study, thermal properties, mechanical properties, and changes in physical properties after irradiation were analyzed after manufacturing a composite material by adding copper and tungsten to F82H steel, one of the RAFM steels. Each composite material was manufactured by putting Cu or W wire into F82H powder produced by gas atomizing and sintering by using a spark plasma sintering (SPS) at temperatures of 850 °C and 1000 °C, respectively. After the SPS, all specimens were annealed at 800 ℃ for 180 min for the heat treatment. The measurements for densities by using Archimedes' method and for the thermal diffusivities by a laser flash analysis (LFA). And then, the thermal conductivity of each specimen was calculated by using the density obtained from Archimedes' method, and the thermal diffusivity and the specific heat data obtained from the LFA. For the surface structure observation, scanning electron microscope (SEM), and energy dispersive spectroscopy

(EDS) were conducted for SPSed and annealed samples. Mechanical property examinations were performed to compare between general F82H and SPSed F82H-based composite materials. With the SPS holding at 850 °C for 10 min to 120 min, the composite materials show very poor mechanical properties, such as tensile property and Vickers hardness. The reason for the F82H-based composite material showed low mechanical properties is that the relative density was lowered, and pores were generated inside the material because the sintering temperature was not high enough and the sintering was not performed properly inside the F82H. In order to increase the relative density, the temperature increase rate was lowered from 100 °C/min to 50 °C/min, but the sintering temperature of 850 °C was increased to 1000 °C.

The F82H-based composite material sintered at a temperature of 1000°C showed a thermal conductivity improvement of up to 3.3 times compared to the existing F82H. However, in the composite material containing W, as the volume fraction of W increased, the ductility of the composite material significantly decreased, resulting in very low toughness. The reason for this result is related that the formation of intermetallic compounds, such as Fe_7W_6, Fe_3W_3C and Fe_2W phases could be found between tungsten and matrix in sintered steels. F82H-W reaction layer surrounding W wire, Fe_7W_6 intermetallic compounds would occur the embrittlement of entire elongation and initiation of fracture during the tensile test. In contrast, F82H-20Cu composite material showed no separation or crack initiation at the interface between F82H and copper wire, resulted in a satisfactory tensile property. From those results, F82H-20Cu composite material SPSed at 1000 °C for 120 min is suggested that the optimized condition to improve the thermal conductivity, leading to a comparable tensile property with that of the general F82H.

In the case of material embrittlement, the most important area to focus on is the evaluation of the investigation characteristics and the establishment of a database. It is almost impossible to evaluate the effect of He or H generated by nuclear transformation under high-energy neutron irradiation on low-temperature fracture toughness or high-temperature creep, using an irradiation test using a nuclear fission reactor. In this regard, the effect of He has been indirectly evaluated through the method using He ion implantation. Irradiation damage modeling has long been an important issue in that it supplements the limitations of long-term irradiation tests by predicting various causes and results of material damage. For triple ion beam irradiated F82H-composite materials, F82H-20W composite material shows higher irradiation hardening than that of F82H-20Cu composite material. Cu part in F82H-20cu shows no irradiation hardening for the irradiation at 500 °C. F82H-W reaction layer with the F82H-W reaction layer tends to larger increase hardening for the irradiation condition. Radiation-induced dislocation loop was not observed in F82H after ion irradiation at 500 °C. For these reasons, F82H-Cu composite could be a candidate material for divertor of fusion reactor, especially at higher temperature.

Contents

Contents IV

List of Figures VI

List of Tables IX

Chapter 1 – Introduction 1

1.1 New Generation Energy System 2

1.2 Requirements for Nuclear Fusion Reactor 7

1.3 Candidates of Structural Materials for Nuclear Fusion Reactor 10

1.4 Composite Material 13

1.5 Objective 14

References 15

Chapter 2 – Experimental Method 23

2.1 Specimen fabrication by using Spark Plasma Sintering 24

2.2 Archimedes' Principle and Density Determination 27

2.3 Laser Flash Analysis 28

2.4 Thermal simulation 29

2.5 Scanning Electron Microscopy 30

2.6 Mechanical Properties Analysis for Bulk Materials 32

2.6.1 Tensile Test 32

2.6.2 Vickers Hardness Test 33

2.6.3 Nano-indentation 34

2.7 Transmission Electron Microscopy 35

2.8 Ion Irradiation 36

References 37

Chapter 3 – Fabrication of F82H-based composites 39
3.1 Introduction 40
3.2 F82H-based composite materials SPSed at 850 °C and 1000 °C 42
3.2.1 Relative Densities and Thermal Conductivities of F82H Composites SPSed at 850 °C 42
3.2.2 Relative Densities and Thermal Conductivities of F82H Composites SPSed at 1000 °C 45
3.3 Microstructure of F82H-based composite materials 47
3.3.1 Microstructure of F82H-based composite materials SPSed at 850 °C 47
3.3.2 Microstructure of F82H-based composite materials SPSed at 1000 °C 49
3.4 Tensile property of F82H-based composite materials 52
3.5 Summary 58
References 61
Chapter 4 – Microstructure analysis in irradiated RAFM and F82H composite materials 62
4.1 Introduction 63
4.2 Microstructure analysis for irradiated RAFM 65
4.3 Microstructure analysis for irradiated F82H composite materials 71
References 81
Chapter 5 – Discussion 83
5.1 Differences of irradiation conditions between RAFM and F82H composite materials. 84
5.2 Irradiation Hardening 86
5.3 Thermal simulation 93
5.3 Summary 95
References 96
Chapter 6 – Conclusion 98

List of Figures

Figure 1.1 Consumption-based CO_2 emissions per capita vs GDP per capita [3] 3

Figure 1.2 Schematic image of a nuclear fusion reaction..... 5

Figure 1.3 The design of ITER..... 6

Figure 2.1 Conceptional design model of SPS 25

Figure 2.2 3D Concept model of F82H-*x*W-*y*Cu composites..... 29

Figure 2.3 Shape of micro-tensile test specimen (Type SS-J1) 32

Figure 3.1 Thermal conductivities and relative densities of F82H-*x*W-*y*Cu composites SPSed at 850 °C 44

Figure 3.2 Thermal conductivities and relative densities of F82H-xW-yCu composites under diverse SPS conditions at 1000 °C 46

Figure 3.3 (a) surface of 15W-5Cu composite SPSed at 850 ℃ for 10 min and (b) Cu wire surrounded by F82H matrix and pores 47

Figure 3.4 Surface of (a), (c) 15W-5Cu and (b), (d) 5W-15Cu composites SPSed at 850 ℃ for 120 min 48

Figure 3.5 Cross-sectional SEM images of F82H-20Cu, F82H-10W-10Cu and F82H-20W composites with 10 to 120 min SPS holding time 50

Figure 3.6 Surface of electro-polished F82H part in F82H-20W composite material..... 50

Figure 3.7 The reaction layer at the interface between F82H and W 51

Figure 3.8 stress–strain curves of sintered F82H, F82H-5W-15Cu, F82H-10W-10Cu and F82H-5W-10Cu composites 52

Figure 3.9 SEM image and EDS mapping images at the fracture surface of the F82H-5W-15Cu after tensile test 53

Figure 3.10 Engineering stress-strain curves on F82H-based composites SPSed at the temperature of 1000 °C 54

Figure 3.11 SEM images and EDS mapping data of fracture surfaces on F82H-20W (a–c), F82H-10W-10Cu (d–f) and F82H-20Cu (g–h) composites with 120 min SPS holding time..... 56

Figure 4.1 Surface structures of RAFM steels used in this chapter..... 66

Figure 4.2 SRIM prediction profile for depth distribution of displacement damage for 6.4 MeV Fe^{3+} ions..... 66

Figure 4.3 Microstructures in Fe^{3+} ion irradiated RAFM steels 67

Figure 4.4 Weak beam dark-field TEM micrographs of microstructures in Fe^{3+} ion irradiated RAFM steels..... 68

Figure 4.5 Dislocation loop distribution in ion-irradiated RAFM steels..... 69

Figure 4.6 Dislocation loop distribution in ion-irradiated RAFM steels..... 69

Figure 4.7 Dislocation loop distribution in ion-irradiated RAFM steels..... 70

Figure 4.8 SRIM prediction profile of depth distribution of displacement damage for 10.5 MeV Fe3+ ions (Blue) and implanted ions for 1.05 MeV He+ ions and 0.38 MeV H+ ions (Red) 72

Figure 4.9 Dislocation loops with ‘coffee bean’ contrast at 1600 nm depths in F82H irradiation at 350 °C 73

Figure 4.10 (a) The low-magnification TEM micrograph and high-magnification microstructure at (b) 800 nm and (c) 1600 depths in F82H irradiation at 350 °C... 73

Figure 4.11 Dislocation loops with ‘coffee bean’ contrast at 1600 nm depths in F82H

irradiation at 350 °C 74

Figure 4.12 conceptional image of the specimen preparation by using FIB 75

Figure 4.13 (a) In-focused microstructure of the F82H-20W composite after the ion-irradiation. (b) Under-focused TEM image over the depth range of 1000 nm to 1800 nm 77

Figure 4.14 (a) In-focused microstructure of the F82H-20Cu composite after the ion-irradiation. (b) Cu part and (c) F82H part in F82H-20Cu composite of under-focused TEM image over the depth range of 1000 nm to 1800 nm 78

Figure 4.15 In-focused microstructure of the F82H-W reaction layer after the ion-irradiation and Under-focused TEM image over the depth range of 1100 nm to 1600 nm 79

Figure 4.16 Size distributions of irradiation-induced cavities at (a)-(b) F82H areas in F82H-W and F82H-Cu composite materials and (c)-(d) the F82H-W reaction layer 79

Figure 5.1 Microstructure of F82H irradiated for triple ion beam at 500 °C 85

Figure 5.2 The dependence of swelling of F82H steels on irradiation temperature [9] .. 85

Figure 5.3 (a) The depth profiles of the averaged nanoindentation hardness on (a) F82H-20W and (b) F82H-20Cu before (△ mark) / after (○ mark) the ion irradiation 87

Figure 5.4 Nix-Gao plot for (△ mark) unirradiated and (△ mark) ion-irradiated (a) F82H-20W and (b) F82H-20Cu 90

Figure 5.5 Overestimation of the value of nano-hardness in various unirradiated materials [10] 92

Figure 5.6 Temperature distribution in (a) F82H, (b) F82H including 1 vol.% pores, (c) F82H-20W and (d) F82H-20Cu 93

List of Tables

Table 3.1 Thermal conductivities and relative densities of composite materials SPSed at 850 °C 43

Table 3.2 Thermal conductivities and relative densities of composite materials SPSed at 1000 °C 46

Table 3.3 Tensile properties of composite materials SPSed at 1000 °C 55

Table 4.1 Chemical compositions of reference RAFM steels 65

Table 4.2 Ion irradiation conditions for reference RAFM steels 65

Table 4.3 Mean dislocation loop diameter and density in RAFM steels irradiated at 325 °C 68

Table 4.4 Mean cavity diameter, number density and swelling fraction in He implanted RAFM steels 70

Table 4.5 Mean cavity diameter, number density and swelling fraction in F82H composites irradiated at 350 °C 75

Table 4.6 The number density and diameter of root mean cube of cavities formed in F82H-based composite materials irradiated at triple ion-beam conditions 80

Table 5.1 H_0 and irradiation induced hardness changes of F82H-20W and F82H-20Cu composite material 89

Table 5.2 Simulated average temperature of composite materials 94

Chapter 1

Introduction

1.1 New Generation Energy System

The biggest cause of global warming, a major concern today, is the increase in carbon dioxide (CO_2) produced by the combustion of fossil fuels, followed by cooling aerosols and cement manufacturing [1]. As an indirect effect of climate change, it has been shown to intensify air pollution, such as increasing ozone concentration, by promoting photochemical reactions in the atmosphere in proportion to the increase in temperature and affecting health. Diseases are increasing through rising global temperatures are also contributing to droughts and increased forest fires [2]. Deforestation can also lead to a rise in temperature over the centuries, change the life cycle of the planet, and even change human civilization. For this reason, many theories for solving human-induced climate change have been widely debated for a long time. Accordingly, many countries around the world have agreed to the 'Paris Agreement' adopted in 2015 and 'An IPCC special report on the impacts of global warming of 1.5 °C' approved at the 45th General Assembly of the Intergovernmental Panel on Climate Change (IPCC) in 2018 [3-4]. According to the proposal, carbon neutrality is legislated or declared as a goal by 2050. A total change in the economic and social structure is required to realize carbon neutrality [5]. Among them, the most fundamental problem to be solved is the energy source problem as shown in figure 1.1 [6].

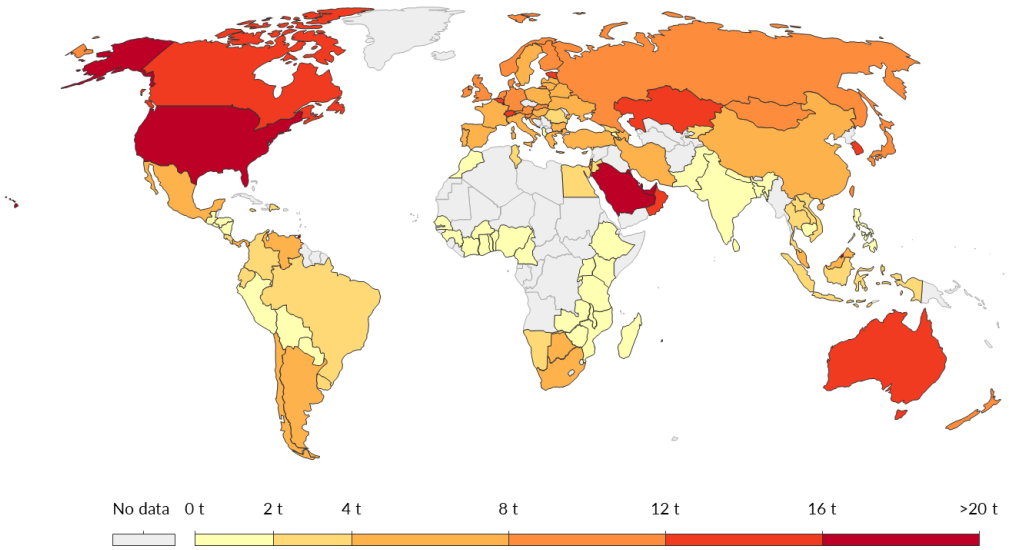

Figure 1.1 Consumption-based CO_2 emissions per capita vs GDP per capita [3]

In order to realize carbon neutrality, the use of fossil fuels should be extremely limited, and the development and share of alternative energy sources that do not generate carbon dioxide should be increased. A nuclear power plant is a place where electricity is generated by using nuclear power [7]. The nuclear reactor acts as a boiler in a thermal power plant that burns coal or oil, and the uranium, the fuel of this reactor, generates two to three neutrons and enormous energy through nuclear fission. The energy released when all 1 gram of uranium is nuclear is equivalent to the energy released when 9 drums of oil or 3 tons of coal are burned [7-8]. Conversely, various fission fragments produced by nuclear fission have very high radioactivity. When a nuclear power plant is in a steady state, these fission fragments cannot escape from the nuclear fuel and are thoroughly protected and shielded, thus, there is no concern about exposure [9]. However, when nuclear fuel is melted and protective and shielding measures are lost, such as in the Chernobyl nuclear power plant or the Fukushima nuclear power plant, a huge amount of radioactive material and powerful radiation can be released into the external environment [8, 10-12]. During the operation of the nuclear power plant, there was a concerning that radiation exposure problems may occur.

In order to use nuclear energy from nuclear fission, thorough and safe measures must be taken to prevent radiation exposure, so it is recognized as a major disadvantage of using nuclear energy. However, there is currently no power generation means to get a large amount of environmentally friendly energy sources that are safe against external shocks such as disasters and fires and do not generate carbon dioxide.

Except for nuclear energy, most of the available energy on Earth is based on solar energy [13-15]. Renewable energies such as solar power and wind power are eco-friendly because they generate almost no carbon dioxide, but there are some limitations in the stable supply of mass energy because there is a large variation depending on the region and environment and the energy generation efficiency is much lower than that of fossil fuel power generation or nuclear power generation [16]. There is the safest and most stable alternative for realizing long-term sustainable carbon neutrality by compensating for the shortcomings of these renewable energies is to implement nuclear fusion energy similar to that of the sun directly on Earth.

Nuclear fusion refers to a reaction in which two light atomic nuclei react to form a heavier atomic nucleus. In the process of overcoming repulsion and fusion into heavier atomic nuclei, energy is generated as much as the reduced mass [17-18]. Nuclear force acts between the protons and neutrons making up the nucleus, and when the distance between each other is closer than 1.0×10^{-14} m, it becomes an attractive force that overcomes the electrical repulsion force (Coulomb's force) between protons with the same charge [19]. When the above conditions are given between relatively light atomic nuclei such as hydrogen or helium, they combine with their attractive force to form heavier atomic nuclei and release binding energy at the same time. Thermonuclear fusion is a method of colliding by using the large thermal velocity of atomic nuclei by making high-temperature plasma into a high-temperature plasma to overcome Coulomb's force and bring atomic nuclei closer together as

shown in figure 1.2 [20].

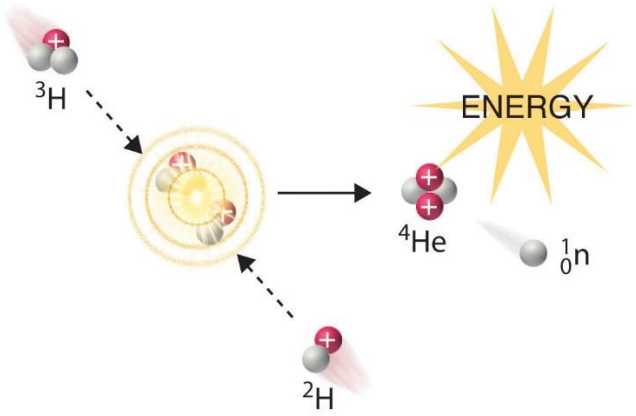

Figure 1.2 Schematic image of a nuclear fusion reaction

Although nuclear fusion energy has been developed since the 1950s, the level of development has risen sharply over the past 20 years, and it has entered the engineering development stage beyond the previous simple basic research stage. The realization of fusion energy, with the highly advanced peripheral technology, is increasingly coming into sight. To demonstrate the production of large-capacity fusion energy, the International Fusion Experimental Reactor (ITER), jointly built by seven leading countries, is about to be completed in 2025. The design of ITER fusion reactor is presented in Fig. 1.3 [21].

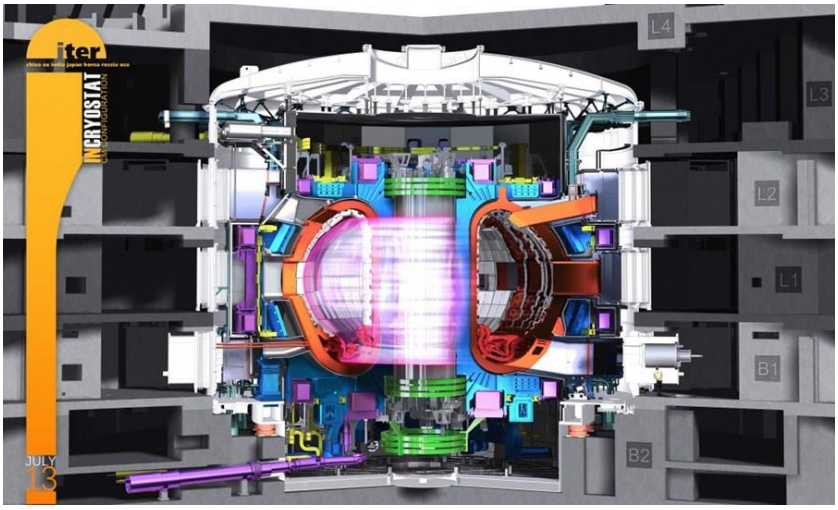

Figure 1.3 The design of ITER

Theoretically, the efficiency of fusion energy is about seven times that of nuclear power, which is the most efficient power generation method at present. A nuclear fusion reaction with 1 kg of hydrogen can produce as much electricity as a thermal power plant using 8 tons of coal. Above all, deuterium, one of the raw materials for power generation, exists close to infinity on Earth, and high-level radioactive waste does not come out during the power generation process. Leading countries in nuclear fusion are proposing specific plans to show electricity production through nuclear fusion. From several years ago, China has already made aggressive investments with the goal of completing a nuclear fusion energy demonstration device in the 2030s [22]. Last year, the UK announced its plan to complete the world's first nuclear fusion power generation demonstration equipment (STEP) in 2040 as one of the 10 key plans for the green industrial revolution [23]. The United States also published a report containing detailed research plans in response to the proposal that nuclear fusion power production should be demonstrated between 2035 and 2040 to achieve carbon neutrality in 2050 [24]. Japan included the development of nuclear fusion energy in its plan to achieve 2050 carbon neutrality [25].

1.2 Requirements for Nuclear Fusion Reactor

The advantage of a fusion reactor is that there is no risk of explosion or serious accident even in an unexpected accident, and high-efficiency energy capable of producing large-capacity electricity can be used in an environmentally friendly manner. However, the fusion reactor is a very complex device in which high-temperature plasma of 100 million °C or higher is confined by a superconducting magnet with a high magnetic field of -270 °C [26]. Element technologies for commercial fusion reactors include core combustion plasma, tokamak devices, and technologies related to energy transport and conversion systems [27]. In particular, vacuum containers and structural materials related to tokamak devices are very important because they must be operated for a long time in an extremely harsh environment.

Blanket and Divertor are representative structural materials for fusion reactors. Most of the energy by deuterium-tritium (D-T) fusion is released in the form of high-energy neutrons of about 14.1 MeV [28-30]. Blanket converts the kinetic energy of this neutron into thermal energy and plays a role in protecting structures such as vacuum vessels and superconducting magnets from neutron irradiation [31]. When a nuclear fusion reaction starts, it creates tritium by itself using the neutrons that result from the reaction. The first wall of the fusion reactor, the blanket, surrounds the inside of the vacuum vessel, the space where the fusion reaction takes place and serves to collect neutrons that are ejected because of the fusion reaction [30, 32].

The high kinetic energy of the neutrons collected in the blanket is converted into thermal energy, which heats the coolant flowing inside the blanket to generate steam, which turns a turbine to produce electricity. When neutrons reach the lithium layer inside the blanket, the lithium and neutrons react to form tritium at the same time. Tritium not used in the fusion

reaction is emitted mixed with impurities, and only tritium is separated and purified from this effluent and stored, so that it can be used again as a fuel for fusion. The divertor protects the vacuum vessel surrounding the outside against the high-temperature heat load (>20 MW/m^2) generated from the internal plasma and removes impurities generated from He alpha particles during nuclear fusion reactor operation [33-35]. Impurities interfere with high-temperature and high-purity plasma generation. Therefore, the Divertor is a major device that minimizes plasma contamination by removing impurities in the core and protects the vacuum vessel and diagnostic equipment from the high temperature of the plasma [36-37].

In a nuclear fusion reactor, various materials are required for each component. In particular, the structural materials located from the plasma to the blanket and diverter must exhibit stable characteristics in a very harsh operating environment, thus selection of appropriate materials and development of reliable structural materials. This becomes a prerequisite for the realization of a highly efficient nuclear fusion reactor. Blanket and Divertor are components exposed to the harshest environment in a fusion reactor due to harsh neutron irradiation, ultra-high temperature, and high magnetic field [38-42]. Therefore, it can be said that the development of structural materials is very important to secure competitiveness in terms of stability, reliability, environment-friendly issues, and unit cost of electricity generation for practical use of fusion power generation.

For the development of a nuclear fusion reactor, various design and analysis methods, such as safety analysis in a high-temperature neutron irradiation environment, must be supported [42]. For these reasons, the structural materials that can withstand harsh environments are essential. In particular, as an increase in the thermal load incident upon plasma operation of a commercial fusion reactor is expected, active cooling between the face-to-face material and the cooling plate is required to secure the safety of the fusion reactor,

and the development of a technology capable of maximally increasing heat transfer is required.

1.3 Candidates of Structural Materials for Nuclear Fusion Reactor

Ferritic martensitic steel (FM steel) with a martensitic microstructure with iron (Fe) as the base and chromium (Cr) as the main alloying element is already used in thermal power plants, etc., has high resistance to void swelling and he embrittlement [43-44]. However, it has the advantage of excellent compatibility with coolants, such as liquid metals. Due to the decrease in creep strength, the operating temperature is limited to about 550°C, irradiation embrittlement is brittle due to high-speed neutron irradiation at temperatures below 400°C, and the BCC crystal structure with the magnetic properties, thus it is difficult to design. In nuclear structural materials, nuclear fission or fusion reactors do not produce highly radioactive materials. However, when high-energy neutrons are absorbed by non-fissile core components or structural materials, the absorbed atoms are converted, and radioactive isotopes are generated [45]. This radioactive element decays into stable isotopes, accompanied by the emission of β or γ radiation. Depending on the element, radiation continues to be emitted for a long period after irradiation is complete. Radiation is an important issue for safety and daily operation, decomposition of power plants, and disposal of radioactive waste. In addition, the material applied to the fusion reactor must maintain sufficient toughness and high-temperature strength during use at high temperatures and resistance to irradiation damage caused by high-energy neutron irradiation. FM steel has problems such as irradiation hardening at low temperatures, significant increase in the Charpy ductile-brittle transition temperature (DBTT) or reduction of fracture toughness, and changes in fracture properties due to helium and hydrogen. There is a problem, and studies are being actively conducted to solve it. Accordingly, there are two important considerations in the development of fusion reactor materials. First, it suppresses the addition of molybdenum (Mo), niobium (Nb), nickel (Ni), etc., which have radioactive properties, and

instead tungsten (W), vanadium (V), manganese (Mn), Tantalum (Ta) and titanium (Ti) are added. The other is to remove impurities that affect induced activation and dose rate as much as possible, even when a small amount is added [46-48]. By manufacturing reduced activation ferritic martensitic (RAFM) steels such as EUROFER 97 in Europe, F82H steel in Japan and CLAM in China, a database for the evaluation of properties in the fusion reactor operating environment has established and manufacturable has evaluated [49-51].

Tungsten, as a candidate material for the fusion reactor plasma, has excellent refractory properties and resistance to surface erosion [52-55]. However, using pure tungsten as a material for a fusion reactor diverter has a serious problem because it becomes brittle by recrystallization and irradiation. When the material becomes brittle like this, cracks in the structure cause air to enter, and tungsten produces radioactive oxides. The problem of tungsten embrittlement must be addressed because the generated radioactive oxides pose a serious safety risk if they are released. In recent years, research on developing alloys or composite materials based on tungsten has been extensively conducted. Tungsten, a material with excellent heat/erosion resistance, is considered as a plasma-facing material for the first wall and divertor in the center, which must be in contact with high-energy (14.1 MeV) neutrons and high-temperature plasma. Since tungsten (W) or tungsten alloys have a large atomic number, erosion by plasma in the operating state of a nuclear fusion reactor is significantly less than that of a low atomic number material [56-57]. Therefore, tungsten-based alloys stand out as structural materials that exhibit high durability that can withstand long-term conditions under heat and deuterium particle erosion at high temperatures [57].

Unlike tungsten, which is a major candidate for plasma facing materials, copper-based alloys such as CuNiBe alloys and CuCrZr alloys are mainly mentioned as divertor structural materials [58-60]. The high thermal conductivity of the copper alloy allows it to transfer high heat loads from the plasma to the cooling tube. Copper inherently has a high thermal

conductivity of about 380 W/(m•k) at between 20 - 500 °C, which results in high heat flux characteristics [60]. Copper-based precipitation hardened (PH) copper alloys and dispersion strengthened (DS) copper alloys typically have a thermal conductivity of about 80-90% of pure copper [61-64]. The Cu-Ni-Be alloy has a rather low thermal conductivity, accounting for 65-75% of pure copper [65]. Since it is higher than F82H having a thermal conductivity of 31.3 W/(m•k) or tungsten having a thermal conductivity of 173 W/(m•k), it is one candidate for application to a location with a very high heat flux among fusion reactor structural materials [65-67].

1.4 Composite Material

The dissimilar material joining technology is one of the most important material technologies for the realization of a nuclear fusion reactor [68]. For the development of nuclear fusion reactors and fusion-related technologies, in terms of materials, materials that face high-temperature plasma, materials that transmit generated thermal energy, and structural materials should be developed separately. However, in the entire manufacturing process of a fusion reactor, these dissimilar materials are joined to form a single part, so dissimilar material bonding technology is an essential element technology that must be secured for the construction of a fusion reactor [69]. Composite material is the product made through this dissimilar material bonding technology. Composite material refers to a material having an effective function by macroscopically combining two or more types of materials with different components or properties [68, 70-72]. Alloys in which two or more types of materials are microscopically combined and have macroscopic homogeneity are not referred to as composite materials. Unlike alloys, composites have macroscopic interfaces between their constituent materials. Components of composite materials include fibers, particles, lamina, and matrix [73]. Composite materials composed of these elements can be classified into layered composites, particle-reinforced composites, fiber-reinforced composites.

1.5 Objective

The major objective of this study is improving the thermal conductivity of F82H by adding W or Cu in the matrix. Each composite material was manufactured by putting Cu or W wire into F82H powder produced by gas atomizing and sintering by using a spark plasma sintering (SPS). In order to fabricate a dense composite material, it is most important to find the optimal SPS condition. After fabricating several candidate composite materials, it is essential to compare and analyze changes in thermal conductivity, mechanical properties, and irradiation properties with the existing F82H.

References

[1] The Intergovernmental Panel on Climate Change (IPCC), Fifth Assessment Report, 2014

[2] O'Neill, S., Williams, H. T., Kurz, T., Wiersma, B., & Boykoff, M. (2015). Dominant frames in legacy and social media coverage of the IPCC Fifth Assessment Report. Nature Climate Change, 5(4), 380-385.

[3] MASSON-DELMOTTE, Valérie, et al. Global warming of 1.5 C. An IPCC Special Report on the impacts of global warming of, 2018, 1.5.

[4] Chepeliev M, van der Mensbrugghe D. Global fossil-fuel subsidy reform and Paris Agreement. Energy Economics. 2020 2020/01/01/;85:104598

[5] Soutter ARB, Mõttus R. "Global warming" versus "climate change": A replication on the association between political self-identification, question wording, and environmental beliefs. Journal of Environmental Psychology. 2020 2020/06/01/;69:101413 ISE

[6] Vaclav Smil. Energy Transitions: Global and National Perspectives. & BP Statistical Review of World Energy, 2017

[7] HEWITT, Geoffrey Frederick; COLLIER, John G. Introduction to nuclear power. CRC Press, 2000.

[8] Deutch, J., Moniz, E., Ansolabehere, S., Driscoll, M., Gray, P., Holdren, J., ... & Todreas, N. (2003). The future of nuclear power. an MIT Interdisciplinary Study, http://web. mit. edu/nuclearpower.

[9] DAVIS, Lucas W. Prospects for nuclear power. Journal of Economic perspectives,

2012, 26.1: 49-66.

[10] RAMANA, M. V. Nuclear power and the public. Bulletin of the Atomic Scientists, 2011, 67.4: 43-51.

[11] HATCH, M., et al. The Chernobyl disaster: cancer following the accident at the Chernobyl nuclear power plant. Epidemiologic reviews, 2005, 27.1: 56-66.

[12] BUESSELER, Ken; AOYAMA, Michio; FUKASAWA, Masao. Impacts of the Fukushima nuclear power plants on marine radioactivity. Environmental science & technology, 2011, 45.23: 9931-9935.

[13] PANWAR, N. L.; KOTHARI, Richa; TYAGI, V. V. Thermo chemical conversion of biomass–Eco friendly energy routes. Renewable and Sustainable Energy Reviews, 2012, 16.4: 1801-1816.

[14] HOFFERT, Martin I., et al. Advanced technology paths to global climate stability: energy for a greenhouse planet. science, 2002, 298.5595: 981-987.

[15] VALENTA, Christopher R.; DURGIN, Gregory D. Harvesting wireless power: Survey of energy-harvester conversion efficiency in far-field, wireless power transfer systems. IEEE Microwave Magazine, 2014, 15.4: 108-120.

[16] ATIA, Raji; YAMADA, Noboru. Sizing and analysis of renewable energy and battery systems in residential microgrids. IEEE Transactions on Smart Grid, 2016, 7.3: 1204-1213.

[17] FLEISCHMANN, Martin; PONS, Stanley; HAWKINS, Marvin. Electrochemically induced nuclear fusion of deuterium. Elsevier Sequoia, 1989.

[18] MIYAMOTO, Kenro. Plasma physics for nuclear fusion. Cambridge, 1980.

[19] KRANE, Kenneth S., et al. Introductory nuclear physics. New York: Wiley, 1988.

[20] MARTIN, Brian R.; SHAW, Graham. Particle physics. John Wiley & Sons, 2017.

[21] AYMAR, R.; BARABASCHI, P.; SHIMOMURA, Y. The ITER design. Plasma physics and controlled fusion, 2002, 44.5: 519.

[22] WAN, Yuanxi, et al. Overview of the present progress and activities on the CFETR. Nuclear Fusion, 2017, 57.10: 102009.

[23] GIBNEY, Elizabeth. UK hatches plan to build world's first fusion power plant. Nature, 2019.

[24] PEARSON, Richard J.; ANTONIAZZI, Armando B.; NUTTALL, William J. Tritium supply and use: a key issue for the development of nuclear fusion energy. Fusion Engineering and Design, 2018, 136: 1140-1148.

[25] MURAOKA, K., et al. Short-and long-range energy strategies for Japan and the world after the Fukushima nuclear accident. Journal of Instrumentation, 2016, 11.01: C01082.

[26] POST, Douglass Edmund; BEHRISCH, Rainer. Physics of plasma-wall interactions in controlled fusion. Springer Science & Business Media, 2013.

[27] NAJMABADI, Farrokh, et al. Overview of the ARIES-RS reversed-shear tokamak power plant study. Fusion Engineering and Design, 1997, 38.1-2: 3-25.

[28] PARISH, T. A.; DAVIDSON, J. W. Reduction in the toxicity of fission product wastes through transmutation with deuterium-tritium fusion neutrons. Nuclear Technology, 1980, 47.2: 324-342.

[29] MARTIN, A. J.; SIMMS, R. J.; JACOBS, R. B. Beta energy driven uniform deuterium–tritium ice layer in reactor-size cryogenic inertial fusion targets. Journal of Vacuum Science & Technology A: Vacuum, Surfaces, and Films, 1988, 6.3: 1885-1888.

[30] ŞAHIN, Sümer; AL-KUSAYER, Tawfik A.; RAOOF, Muhammad Abdul. Preliminary design studies of a cylindrical experimental hybrid blanket with deuterium-

tritium driver. Fusion Technology, 1986, 10.1: 84-99.

[31] ABDOU, M. A.; CONN, Robert W. A comparative study of several fusion reactor blanket designs. Nuclear Science and Engineering, 1974, 55.3: 256-266.

[32] KLEYN, A. W.; CARDOZO, NJ Lopes; SAMM, U. Plasma–surface interaction in the context of ITER. Physical Chemistry Chemical Physics, 2006, 8.15: 1761-1774.

[33] RAFFRAY, A. R., et al. Engineering design and analysis of the ARIES-CS power plant. Fusion Science and Technology, 2008, 54.3: 725-746.

[34] AKIBA, M., et al. Development of high heat flux components in JAERI. In: 18th IEEE/NPSS Symposium on Fusion Engineering. Symposium Proceedings (Cat. No. 99CH37050). IEEE, 1999. p. 381-384.

[35] LI, Muyuan; YOU, Jeong-Ha. Interpretation of the deep cracking phenomenon of tungsten monoblock targets observed in high-heat-flux fatigue tests at 20 MW/m2. Fusion Engineering and Design, 2015, 101: 1-8.

[36] PARKER, R., et al. Plasma-wall interactions in ITER. Journal of Nuclear Materials, 1997, 241: 1-26.

[37] COHEN, Samuel Alan. Vacuum and wall problems in precursor reactor tokamaks. Journal of Vacuum Science and Technology, 1976, 13.1: 449-462.

[38] STORK, D.; ZINKLE, S. J. Introduction to the special issue on the technical status of materials for a fusion reactor. Nuclear Fusion, 2017, 57.9: 092001.

[39] GILBERT, M. R., et al. An integrated model for materials in a fusion power plant: transmutation, gas production, and helium embrittlement under neutron irradiation. Nuclear Fusion, 2012, 52.8: 083019.

[40] FEDERICI, G., et al. European DEMO design strategy and consequences for materials. Nuclear Fusion, 2017, 57.9: 092002.

[41] ABDOU, Mohamed, et al. Blanket/first wall challenges and required R&D on the pathway to DEMO. Fusion Engineering and Design, 2015, 100: 2-43.

[42] LINSMEIER, Ch, et al. Development of advanced high heat flux and plasma-facing materials. Nuclear Fusion, 2017, 57.9: 092007.

[43] FOREMAN, A. J. E.; MAKIN, M. J. Dislocation movement through random arrays of obstacles. Canadian Journal of Physics, 1967, 45.2: 511-517.

[44] PATEL, J. R.; COHEN, Morris. Criterion for the action of applied stress in the martensitic transformation. Acta metallurgica, 1953, 1.5: 531-538.

[45] BOWMAN, C. D., et al. Nuclear energy generation and waste transmutation using an accelerator-driven intense thermal neutron source. Nuclear Instruments and Methods in Physics Research Section A: Accelerators, Spectrometers, Detectors and Associated Equipment, 1992, 320.1-2: 336-367.

[46] VAN DER SCHAAF, B., et al. Progress and critical issues of reduced activation ferritic/martensitic steel development. Journal of Nuclear Materials, 2000, 283: 52-59.

[47] WANG, Xu, et al. Void swelling in high dose ion-irradiated reduced activation ferritic–martensitic steels. Journal of Nuclear Materials, 2015, 462: 119-125.

[48] CABET, C., et al. Ferritic-martensitic steels for fission and fusion applications. Journal of Nuclear Materials, 2019, 523: 510-537.

[49] FERNÁNDEZ, P., et al. Metallurgical characterization of the reduced activation ferritic/martensitic steel Eurofer'97 on as-received condition. Fusion Engineering and Design, 2001, 58: 787-792.

[50] JITSUKAWA, S., et al. Development of an extensive database of mechanical and physical properties for reduced-activation martensitic steel F82H. Journal of Nuclear Materials, 2002, 307: 179-186.

[51] HUANG, Qunying, et al. Development status of CLAM steel for fusion application. Journal of Nuclear Materials, 2014, 455.1-3: 649-654.

[52] DAVIS, J. W., et al. Assessment of tungsten for use in the ITER plasma facing components. Journal of nuclear materials, 1998, 258: 308-312.

[53] WURSTER, S., et al. Recent progress in R&D on tungsten alloys for divertor structural and plasma facing materials. Journal of Nuclear Materials, 2013, 442.1-3: S181-S189.

[54] KNASTER, J.; MOESLANG, A.; MUROGA, T. Materials research for fusion. Nature Physics, 2016, 12.5: 424-434.

[55] HU, Xunxiang, et al. Irradiation hardening of pure tungsten exposed to neutron irradiation. Journal of Nuclear Materials, 2016, 480: 235-243.

[56] MARIAN, Jaime, et al. Recent advances in modeling and simulation of the exposure and response of tungsten to fusion energy conditions. Nuclear Fusion, 2017, 57.9: 092008.

[57] RIETH, M., et al. Recent progress in research on tungsten materials for nuclear fusion applications in Europe. Journal of Nuclear Materials, 2013, 432.1-3: 482-500.

[58] PHILIPPS, V. Tungsten as material for plasma-facing components in fusion devices. Journal of nuclear materials, 2011, 415.1: S2-S9.

[59] SINGH, B. N., et al. Effects of heat treatments and neutron irradiation on microstructures and physical and mechanical properties of copper alloys. Journal of nuclear materials, 1997, 249.1: 1-16.

[60] KALININ, G.; MATERA, R. Comparative analysis of copper alloys for the heat sink of plasma facing components in ITER. Journal of nuclear materials, 1998, 258: 345-350.

[61] ZINKLE, S. J.; FABRITSIEV, S. A. Copper alloys for high heat flux structure applications. Atomic and Plasma-Material Interaction Data for Fusion (supplement to Nuclear Fusion), 1994, 5: 163.

[62] SINGH, B. N.; EDWARDS, D. J.; TOFT, P. Effects of neutron irradiation on mechanical properties and microstructures of dispersion and precipitation hardened copper alloys. Journal of nuclear materials, 1996, 238.2-3: 244-259.

[63] BARABASH, V. R., et al. Specification of CuCrZr alloy properties after various thermo-mechanical treatments and design allowables including neutron irradiation effects. Journal of nuclear materials, 2011, 417.1-3: 904-907.

[64] ZINKLE, Steven J. Applicability of copper alloys for DEMO high heat flux components. Physica Scripta, 2015, 2016.T167: 014004.

[65] LI, Meimei; SOKOLOV, M. A.; ZINKLE, S. J. Tensile and fracture toughness properties of neutron-irradiated CuCrZr. Journal of nuclear materials, 2009, 393.1: 36-46.

[66] ROTEM, A.; SHECHTMAN, D.; ROSEN, A. Correlation among microstructure, strength, and electrical conductivity of Cu-Ni-Be alloy. Metallurgical Transactions A, 1988, 19.9: 2279-2285.

[67] MAKINSON, R. E. B. The thermal conductivity of metals. In: Mathematical Proceedings of the Cambridge Philosophical Society. Cambridge University Press, 1938. p. 474-497.

[68] KLEMENS, P. G.; WILLIAMS, R. K. Thermal conductivity of metals and alloys. International metals reviews, 1986, 31.1: 197-215.

[69] CLYNE, Trevor William; HULL, Derek. An introduction to composite materials. Cambridge university press, 2019.

[70] JONES, Russell H.; HENAGER JR, Charles H.; HOLLENBERG, Glenn W.

Composite materials for fusion applications. Pacific Northwest Lab., Richland, WA (United States), 1991.

[71] JONES, Robert M. Mechanics of composite materials. CRC press, 2018.

[72] TSAI, Stephen W.; HAHN, H. Thomas. Introduction to composite materials. Routledge, 2018.

[73] CHRISTENSEN, Richard M. Mechanics of composite materials. Courier Corporation, 2012.

Chapter 2

Experimental Method

2.1 Specimen fabrication by using Spark Plasma Sintering

Sintering refers to the process of powder particles becoming a lump through a thermal activation process. During sintering, the density of the powder compact increases from 40 ~ 60 % to 80 ~ 99.9% after sintering, accompanied by ancillary phenomena [1]. The most representative accompanying phenomenon is a change in particle size, and it is observed that the particle size increases by over 10 times during the sintering process. Therefore, material densification and grain growth are representative sintering phenomena [2]. The sintering process in which densification and grain growth occur is directly related to changes in surface or interfacial energy. The surface area of particles is reduced through densification, and the area of the interface between particles is also reduced through particle growth. This change in energy serves to promote the movement of matter. In addition, chemical synthesis reactions occur simultaneously with densification and grain growth during the sintering process.

In this experiment, spark plasma sintering (SPS) method was applied. Spark plasma sintering is a sintering method with high energy of high-temperature discharge plasma that is instantaneously generated by spark discharge by directly injecting pulse electric energy between the particles of the green compact that are subjected to mechanical pressure [3-5]. Compared to the conventional sintering method by hot press (HP) or hot isostatic press (HIP), SPS is possible at low temperature and for a short time. If HIP is a technology that promotes sintering by applying direct pressure to the specimen with a carbon piston, spark plasma sintering technology promotes sintering by simultaneously applying pressure and current through the carbon holder, as shown in Figure 2.1.

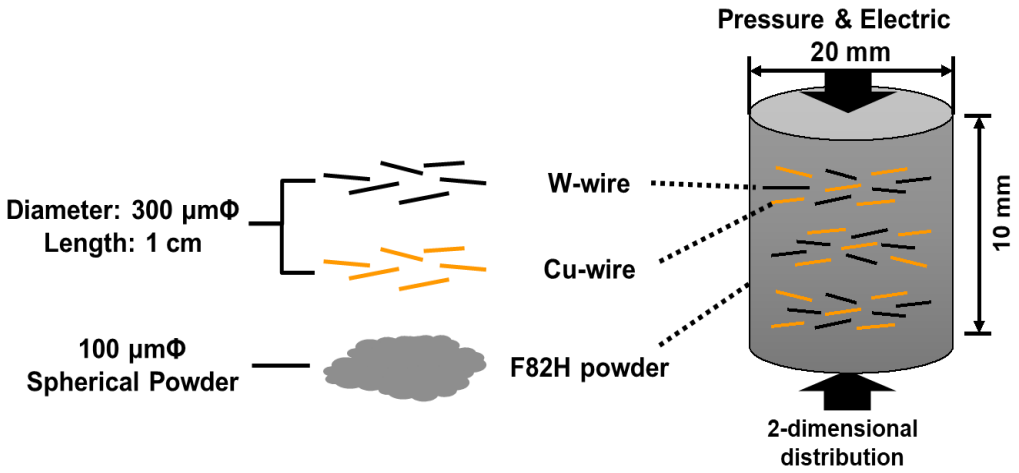

Figure 2.1 Conceptional design model of SPS

It enables sintering even at low temperatures. SPS has the advantage that low-temperature sintering is possible, and thus a sintered body with extremely suppressed grain growth can be manufactured.

To fabricate F82H-based composite materials, F82H powders and wire-shape (1 mm in length and 300 μm in diameter) tungsten (Nippon Tungsten CO., LTD, 99.96% or higher purity) and copper (Nilaco Co., 99.9% purity) are used in this study. The typical compositions of F82H are listed in Table 2.1. About 125 μm sized spherical F82H powders were fabricated by a gas atomization from the bulk F82H. And then, the F82H powders were sintered with tungsten wires and/or copper wires. All the composites were sintered by the SPS (DR.SINTER.LAB, SPS+510 L). The direction of wires was perpendicular to the compression direction for the sintering. In this study, there are two kinds of composite materials with the holding temperature of 850 °C or 1000 °C. To sinter the composite materials at 850 °C, the SPS was performed at the heating rate of 100 °C/min from R.T. to 600°C with 3 min holding time, 50°C/min to 850 °C and then held the temperature under the inner pressure of 40 MPa. Other composites were sintered as the metal volume fraction of

F82H-*x*W-*y*Cu (*x*, *y* = 0~20 vol%). The conceptual model for our study is depicted as shown in Figure 1 (a). The SPS was conducted with the heating rate of 100 °C/min from room temperature to 750°C, and then, 50°C/min until the setting temperature of 1000 °C under the pressure of 40 MPa. The holding time at the highest temperature was 10, 60, and 120 min, respectively. Figure 1 (b) shows the temperature profile applied during the SPS process. The size of SPSed specimens is 20 mm diameters, and the height is about 10 mm. SPSed specimens were machined and cut into a square plate shape with a width of 20 mm, a length of 10 mm, and a thickness of 0.2 mm. And then, the surfaces of each specimen were polished using sandpaper with grits 800, 1000, and 2000 for 6 min, respectively. After cutting and polishing, a heat treatment in the vacuum condition was performed at a temperature of 800 °C for 180 min to reduce the inner stress of the specimens.

2.2 Archimedes' Principle and Density Determination

The state and volume of the material change with temperature. Therefore, accurate temperature measurement must be accompanied by accurate density measurement, and the temperature during measurement must also be kept constant at the same time [6]. In fact, a measurement error of up to 0.0001 g/cm^3 may occur due to a temperature difference of 0.1 °C. Depending on how the volume is defined, it can be divided into true density, appendant density, and bulk density. True density is the density calculated using only the volume of the actual sample except for all pores present inside and outside. It is irrelevant in the case of a densely constructed sample inside, but the true density cannot be measured if there is a waste hole that cannot be accessed from the outside. Apparent density refers to the density calculated using the volume excluding pores open to the outside. That is, since it is the density calculated by dividing the weight of the sample by the volume including the closed pores inside, in the case of a porous material, it is essential to measure the apparent density. Bulk density is the density calculated using the volume including pores open to the outside. In the case of a porous material with micropores, the apparent density and bulk density differ greatly, whereas in the case of an ideal material with no pores and the clear surface, there is no difference between the bulk density and the apparent density. In this experiment, assuming that the density of water is 1 g/m^3, the density was calculated using the dried weight, saturated weight, and suspended weight. The dried weight is the weight of the dried sample, the saturated weight is the weight of the sample in water, and the suspended weight is the weight when the surface of the sample immersed in water is wiped with a damp cloth and the internal pores are filled with water. The relative density was calculated by comparing the density for each sample with the theoretical density, respectively.

2.3 Laser Flash Analysis

The thermal diffusivities of F82H-*x*W-*y*Cu composite materials were measured by the laser flash analysis (Netzsch, LFA 457 MicroFlash). In the conventional contact method for measuring heat conduction in a steady state, there was a problem that an error occurred due to the contact resistance between the sample surface and the heating surface, and it took a lot of time. On the other hand, the flash method, which is a non-contact measurement method, measures the thermal diffusion coefficient without contact resistance with the sample, can measure in a short time, and has the advantages of easy data acquisition and small size of the specimen. The direction of the heat flux during LFA was in the direct path of tungsten and copper wires in the specimens [7-8]. The thermal conductivity of each specimen was calculated by using the density obtained from Archimedes' method, and the thermal diffusivity and the specific heat data obtained from the laser flasher. The specific thermal conductivity could be calculated using the equation of thermal diffusivity:

$$\lambda = \alpha \times C_p \times \rho \tag{2.1}$$

where λ is the specific thermal conductivity, α is the thermal diffusivity, C_p is the specific heat, and ρ is the density [9]. Thermal diffusivity of a material is a thermal property that determines the rate at which heat propagates by its conductivity regarding time at a temperature. The higher the thermal diffusivity, the faster the heat propagates.

2.4 Thermal simulation

For the design of composite materials, thermal simulations with were performed various conditions. The analysis models were designed by using AutoCAD2020 and SpaceClaim as shown in Fig. 2.2. The volume fraction of wires is 20 % of total composite material sample. With designed model, the analysis has been carried out following a theoretical-computational approach based on adopting the commercial computational steady-state thermal analysis code with ANSYS v19.1. The thermal conductivity of each material was set to 31.3 W/(m•k), 173 W/(m•k) and 401 W/(m•k) as F82H, W and Cu.

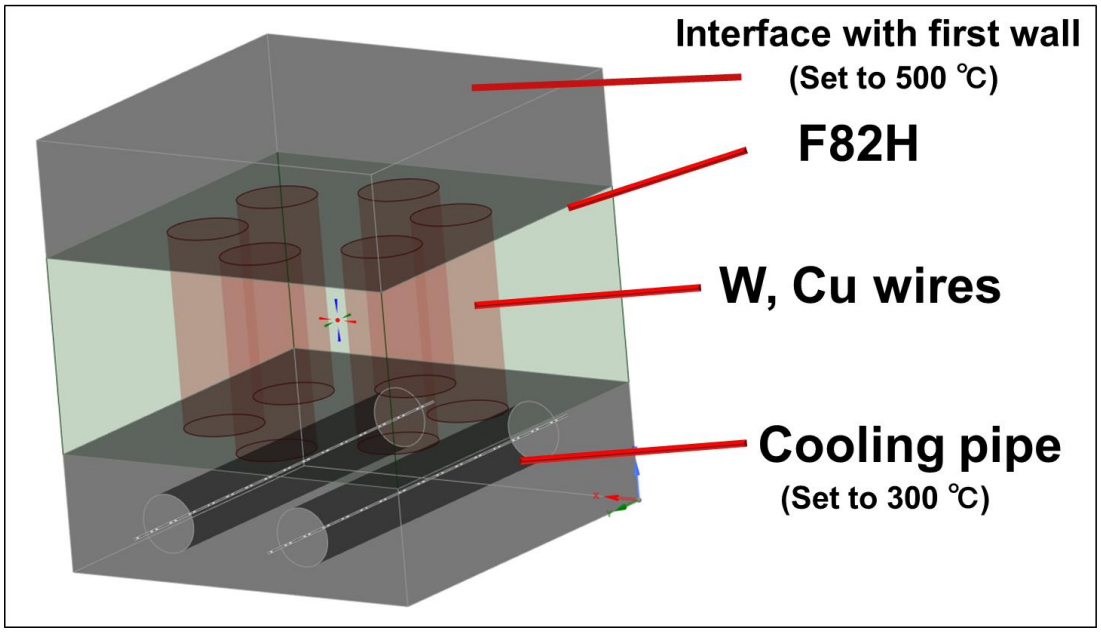

Figure 2.2 3D Concept model of F82H-*x*W-*y*Cu composites

2.5 Scanning Electron Microscopy

A scanning electron microscope (SEM) is a microscope widely used to observe small-sized microstructures and shapes in a solid state. Due to the very small electron beam, it is easy to observe a three-dimensional image with a deep depth of field. Therefore, it is an analysis equipment that can observe three-dimensional shapes, such as complex surface structures and crystal shapes at high magnification [10]. The SEM images information on the reflection or scattering of the electron beam irradiated from the electron gun to the sample, so that the user can analyze the surface of the sample. Secondary Electron (SE) provides detailed information on the surface shape without causing damage to the sample surface due to its relatively low energy [11]. In addition, since the manufacturing cost of the detector is low, and it is easy to control, it is used as a basic detector for SEM. Increasing the accelerating voltage in SE increases the penetration depth of the electron beam, thus decreasing the contrast, but increasing the probability that secondary electrons are emitted from all topologies of the specimen. If higher contrast is required during SEM observation, the contrast can be increased by lowering the acceleration voltage. Electrons that are reflected or scattered from the surface of the sample and then emitted out of the surface of the sample are called back-scattered electrons (BSE), and the detector is often located under the objective lens. Since backscattering increases as the elemental atoms of the sample are heavier, the contrast due to the difference in atomic number appears on the backscattered electrons on the surface of the flat sample. Therefore, information on the composition of the sample can be detected by the backscattered electron image. Energy dispersive spectroscopy (EDS) can be performed with the SEM used in the laboratory. To perform this analysis, SE images are obtained from the program, and X-rays and long-wavelength visible light are detected by the action between primary electrons and solid samples using an EDS detector.

This is a powerful analysis function of SEM that can perform qualitative or quantitative analysis by measuring the distribution of elements by detecting the intensity of characteristic X-rays generated by scanning the primary electron beam on the specimen. For the structure analysis of F82H-based composite materials, surface structure and EDS mapping observation were carried out at 10 to 20 kV using JSM-6510LA scanning electron microscope (SEM, JEOL) equipped with Norman Voyager Series IV (EDS, Thermo Electron Corporation).

2.6 Mechanical Properties Analysis for Bulk Materials

2.6.1 Tensile Test

When conducting a tensile test, the sintered body was processed to a thickness from 0.2 mm to 0.25 mm, and the processed sample was punched out with a punching machine to prepare the SS-J1 micro-tensile test piece as shown in Fig. 2.4. The length of the parallel part of the micro-tensile test piece is 5 mm, and the width is 1.2 mm. For tensile tests, a model-5564 tensile tester manufactured by Instron was used. The tensile test was conducted under the conditions of room temperature, air condition, and strain rate of 10^{-3} s^{-1} [12]. The test was performed at least 5 times for each composite material. Tensile strength and breaking elongation were calculated from the results of the tensile test.

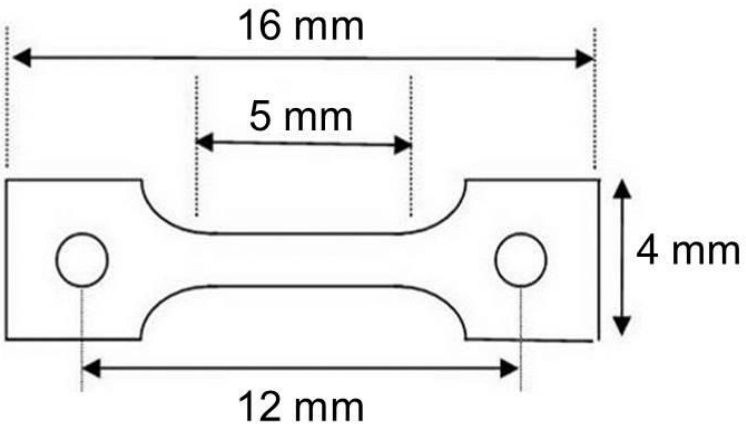

Figure 2.3 Shape of micro-tensile test specimen (Type SS-J1)

2.6.2 Vickers Hardness Test

Vickers hardness tester makes an indentation by pressing a pyramid-shaped diamond indenter with a facing angle of 136°. The hardness expressed as the value obtained by dividing the load by the surface area of the remaining permanent pit is called the Vickers hardness. For Vickers hardness, where the load is P kg and the length of the diagonal of the pit is d mm, then the Vickers hardness Hv becomes $Hv=1.854\ P/d^2$. Since the feet are similar, the hardness value becomes constant regardless of the size of the load. If the size of the load is tiny, the hardness can be measured directly on the surface of the product. Also, the hardness tester that can be used under a load of 1kg or less is called a microhardness tester, and since the pit is very small, it is also used to obtain the hardness distribution of the surface or to measure the hardness of a small part of the material structure [13]. In this study, experiments were performed at room temperature for each region of F82H, W and Cu exposed on the surface. The test load was all the same at 3 kgf, and the test load was maintained for 10 seconds.

2.6.3 Nano-indentation

The nano-indentation tests were performed to evaluate the ion-irradiation-induced mechanical properties. For the F82H-20W and F82H-20Cu composite materials after ion irradiation, the nano-hardness before and after irradiation was measured using the nanoindentation test. The nano-indentation is an analysis technique that measures various mechanical properties such as hardness and elastic modulus by applying a very small load to the surface of an indenter having a certain geometric shape [14-16]. In this experiment, among the tips of various nano indenters such as conical and triangular cylindrical flat punch, the Berkovich tip was used. For the nanoindentation test, progressive multi-cycles in force control were used, and hardness values from 200 nm to 2000 nm depth were measured from the surface of the sample. Unirradiated and irradiated measurement area were tested for Fe, W, and Cu exposed on the surface of the composite material, respectively.

2.7 Transmission Electron Microscopy

The principle of operation of a transmission electron microscope (TEM) is the same as that of an optical microscope, but the light source of the optical microscope is light, whereas the light source of the TEM transmits the specimen with the accelerated electron beam and controls the action of the lens to the full length to control the magnification of the image. Typically, using voltages of up to hundreds of thousands of volts, the electron gun accelerates electrons to high speeds. When accelerated electrons smaller than the wavelength of the material to be observed are generated and transmitted through the medium, a difference in the intensity of the electron beam that can be transmitted occurs depending on the degree of crystal plane or defect. The difference in transmitted beam intensity appears as a contrast to the fluorescent screen. For the microstructure analysis, observation images and diffraction patterns were obtained using a TEM (JEOL, JEOL-2010F) operated at 200 kV. The inner grains of F82H-W-Cu composite materials were observed by bright-field images and weak beam dark-field images.

2.8 Ion Irradiation

It is predicted that the first wall of the fusion reactor will be exposed to neutron irradiation dose of about 300 DPA or more during its service life. It takes almost several decades to irradiate a sample with the above dose in a research reactor. Therefore, ion irradiation using a particle accelerator such as Van de Graaff or cyclotron is widely used where the structural material of a nuclear fusion reactor is damaged during operation. Unlike nuclear reactors, ion irradiation has a high damage density and can cause a large amount of irradiation damage in a short time, making economic research possible. However, in the case of the ion irradiation test, the irradiated damaged area only reaches a depth of several micrometers, thus a nano-micro-scale sample analysis method is indispensable. In this study, triple beam ion irradiation was performed on F82H-20W and F82H-20Cu composite materials sintered at a temperature of 1000 °C. Ion-beam irradiation with 10.5 MeV Fe^{3+}, 1.05 MeV He^{+} and 0.38 MeV H^{+} was performed in perpendicular direction to the polished surfaces at Takasaki Ion Accelerators for Advanced Radiation Application (TIARA) facility in National Institutes for Quantum Science and Technology (QST) [17]. To make a flat ion-concentration peak for He^{+} and H^{+} irradiation, the energy degraders in the accelerator were applied during the irradiation [18]. The irradiation temperature was controlled at the temperature of 500 °C averagely.

References

[1] VINSON, Jack R.; CHOU, Tsu-Wei. Composite materials and their use in structures. 1975.

[2] GERMAN, Randall M. Sintering theory and practice. 1996.

[3] MACKENZIE, J. K.; SHUTTLEWORTH, Ro. A phenomenological theory of sintering. Proceedings of the Physical Society. Section B, 1949, 62.12: 833.

[4] OMORI, Mamoru. Sintering, consolidation, reaction and crystal growth by the spark plasma system (SPS). Materials Science and Engineering: A, 2000, 287.2: 183-188.

[5] MAMEDOV, V. Spark plasma sintering as advanced PM sintering method. Powder Metallurgy, 2002, 45.4: 322-328.

[6] MUNIR, Z. A.; ANSELMI-TAMBURINI, U.; OHYANAGI, M. The effect of electric field and pressure on the synthesis and consolidation of materials: A review of the spark plasma sintering method. Journal of materials science, 2006, 41.3: 763-777.

[7] TAYLOR, Robert P.; MCCLAIN, Stephen T.; BERRY, J. T. Uncertainty analysis of metal-casting porosity measurements using Archimedes' principle. International Journal of Cast Metals Research, 1999, 11.4: 247-257.

[8] COWAN, Robert D. Pulse method of measuring thermal diffusivity at high temperatures. Journal of Applied Physics, 1963, 34.4: 926-927.

[9] BABA, Tetsuya; ONO, Akira. Improvement of the laser flash method to reduce uncertainty in thermal diffusivity measurements. Measurement Science and Technology, 2001, 12.12: 2046.

[10] VOSTEEN, Hans-Dieter; SCHELLSCHMIDT, Rüdiger. Influence of temperature

on thermal conductivity, thermal capacity and thermal diffusivity for different types of rock. Physics and Chemistry of the Earth, Parts A/B/C, 2003, 28.9-11: 499-509.

[11] SUTTON, Michael A., et al. Scanning electron microscopy for quantitative small and large deformation measurements part I: SEM imaging at magnifications from 200 to 10,000. Experimental mechanics, 2007, 47.6: 775-787.

[12] VERNON-PARRY, K. D. Scanning electron microscopy: an introduction. III-Vs Review, 2000, 13.4: 40-44.

[13] HART, E. W. Theory of the tensile test. Acta metallurgica, 1967, 15.2: 351-355.

[14] WAKAI, E., et al. Effect of triple ion beams in ferritic/martensitic steel on swelling behavior. Journal of nuclear materials, 2002, 307: 278-282.

[15] PHARR, G. M.; OLIVER, W. C. Measurement of thin film mechanical properties using nanoindentation. Mrs Bulletin, 1992, 17.7: 28-33.

[16] FISCHER-CRIPPS, Anthony C.; NICHOLSON, D. W. Nanoindentation. Mechanical engineering series. Appl. Mech. Rev., 2004, 57.2: B12-B12.

[17] GANE, N.; COX, J. M. The micro-hardness of metals at very low loads. Philosophical magazine, 1970, 22.179: 0881-0891.

[18] SAITOH, Y., et al. TIARA electrostatic accelerators for multiple ion beam application. Nuclear Instruments and Methods in Physics Research Section B: Beam Interactions with Materials and Atoms, 1994, 89.1-4: 23-26.

Chapter 3

Fabrication of F82H-based composites

3.1 Introduction

The RAFM (Reduced Activation Ferritic / Martensitic) steel is one of the strong candidate materials for the plasma-facing components (PFCs) in demonstration fusion plants (DEMO) nuclear fusion reactor due to its high resistance against the neutron radiation condition. The structural materials in the coolant system and the divertor should have a high thermal conductivity to transfer the high heat load from the plasma-faced region to a coolant pipe. RAFM steels have good mechanical properties at the temperature that the fusion reactor operated and great swelling resistance. However, it has very low thermal conductivity for the structural material of the divertor compared to other candidate materials, such as tungsten or copper-based alloys. Since the SPS temperature of 1000°C is very close to the melting point of copper (1085 °C), it is necessary to pay attention to partial melting of copper during the SPS. Therefore, the temperature increase rate to the holding temperature was set to 50 °C so that the SPS temperature does not exceed the set holding temperature.

A structural material surrounding the coolant for the nuclear fusion reactor is used in harsh environments, for instance, exposed to high-energy neutron flux and concentrations at temperatures of at least 300 °C. Therefore, we had designed one of RAFM steel, F82H-based composite materials to improve the thermal conductivity of the RAFM steels. F82H-*x*W-*y*Cu composite materials (*x*, *y*=0~20 vol.%) were sintered under 40 MPa pressure at 850 °C and 1000 °C for from 10 min to 120 min.

The increase in thermal conductivities of the composites could be expected with the addition of metal wires which have a high thermal conductivity such as pure copper (401 W/(m•k)) and pure tungsten (173 W/(m•k)). The advantage of adding copper is extremely high energy density with very high thermal conductivity. It can make fast removal of the high

heat load from the core region of a reactor to the cooling pipe. However, Cu could be applied at low operating temperatures due to its relatively modest strength parameters. The advantages of adding tungsten are its low coefficient of thermal expansion (CTE), low neutron activation, low tritium retention, and so on. However, a difference of the CTE between tungsten (4.3×10^{-6}/K) and F82H (12×10^{-6}/K) is too large, and it may occur a mechanical failure due to the thermal mismatch or the dimensional instability for an operation of the fusion reactor. Thus, for the F82H-W composite material, it is essential to measure the mechanical properties after sintering, in particular, to analyze the tensile properties.

3.2 F82H-based composite materials SPSed at 850 °C and 1000 °C

3.2.1 Relative Densities and Thermal Conductivities of F82H Composites SPSed at 850 °C

Figure 1 shows the temperature and pressure profile applied during the SPS process. In the SPSed samples, the direction of wires was perpendicular to the compression direction. The composites were sintered as F82H-xW-yCu (x, y = 5~15 vol.%). The conceptual model for our study is depicted as shown in Fig. 2. Samples were cut and machined from the vertical direction, and then the surface of the samples was polished for the laser flash analysis and the microstructural analysis.

The expected thermal conductivity of a composite, $\lambda_{composite}$ was estimated on a basis of the mixture rule [1]. The mixture rule on a thermal conductivity is expressed as below:

$$\lambda_{composite} = \lambda_{matrix} V_{matrix} + \lambda_{additive} V_{additive}$$

where $\lambda_{composite}$ is the sum of thermal conductivity of the matrix and thermal conductivity of the additive, which is directly proportionate to each volume fraction [2]. The relative densities, expected thermal conductivities and actual thermal conductivities of the composite materials are listed in Table 3.1. Figure 3.1 shows the actual thermal conductivities and relative densities of F82H-xW-yCu composites. Assuming F82H-20Cu composite is fully dense, it could have 3 times higher thermal conductivity than F82H bulk. The actual value of the thermal conductivity is a proportional relationship with temperature, thus, the thermal conductivity of F82H-20Cu composite seems to have a lower thermal conductivity than the expected thermal conductivity.

	SPS Holding Time [min]	Expected thermal conductivity [W/mK]	Actual thermal conductivity [W/mK]	Relative density [%]
F82H	-	31.3	31.3	100
F82H+5W+5Cu	10	56.9	43.7	98.7
F82H+5W+10Cu	10	75.4	73.2	96.9
F82H+5W+15Cu	10	93.9	86.8	97.5
F82H+10W+5Cu	10	64.1	56.3	96.3
F82H+10W+10Cu	10	82.5	66.1	96.0
F82H+15W+5Cu	10	71.2	41.6	82.9
F82H+5W+15Cu	60	93.9	82.9	96.4
F82H+15W+5Cu	60	71.2	65.8	98.3
F82H+5W+15Cu	120	93.9	88.6	97.3
F82H+15W+5Cu	120	71.2	67.1	98.6

Table 3.1 Thermal conductivities and relative densities of composite materials

SPSed at 850 °C

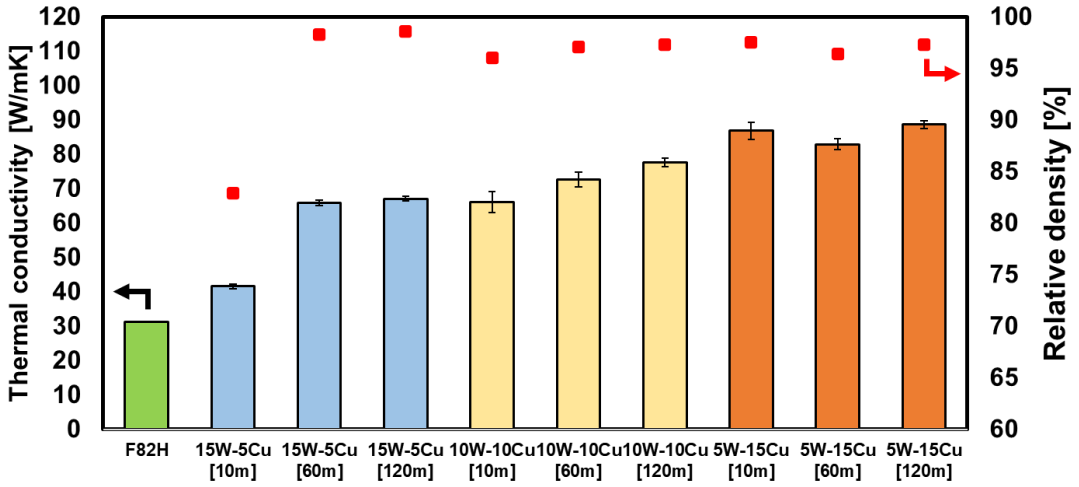

Figure 3.1 Thermal conductivities and relative densities of F82H-*x*W-*y*Cu composites SPSed at 850 °C

3.2.2 Relative Densities and Thermal Conductivities of F82H Composites SPSed at 1000 °C

When a composite is fully dense, it could show the theoretical thermal conductivities, which are their highest thermal conductivity. The expected thermal conductivities of all composites are listed in Table 3.2. And the actual thermal conductivities and the relative densities of the composites were summarized in Fig. 3.2 and Table 3.2. 20 vol.% of tungsten or copper composite material was prepared in order to reduce the variables and problems that may occur by adding tungsten and copper at the same time. Basically, the actual thermal conductivity of a composite would be lower than the expected value calculated by the formula of the mixture rule for a composite material. The theoretical value of the thermal conductivity of F82H-20Cu composite is 105.2 W/(m•k). However, the value of the actual thermal conductivity of F82H-20Cu composite material SPSed at 1000 °C for 120 min was 103.0 W/(m•k) due to its the reduced relative density in SPS and the minute errors that occur in the density measurement. Nevertheless, it was confirmed that the composite material had a very high relative density of 99.8%. In general, in the case of a material sintered with SPS having a relative density of 99% or more, it could be judged that it is well sintered. The problem is the reduced relative density and the minute errors that occur in the density measurement. It is about 3.3 times better thermal conductivity than F82H. As the copper content increases, the amount of increase in thermal conductivity also increases.

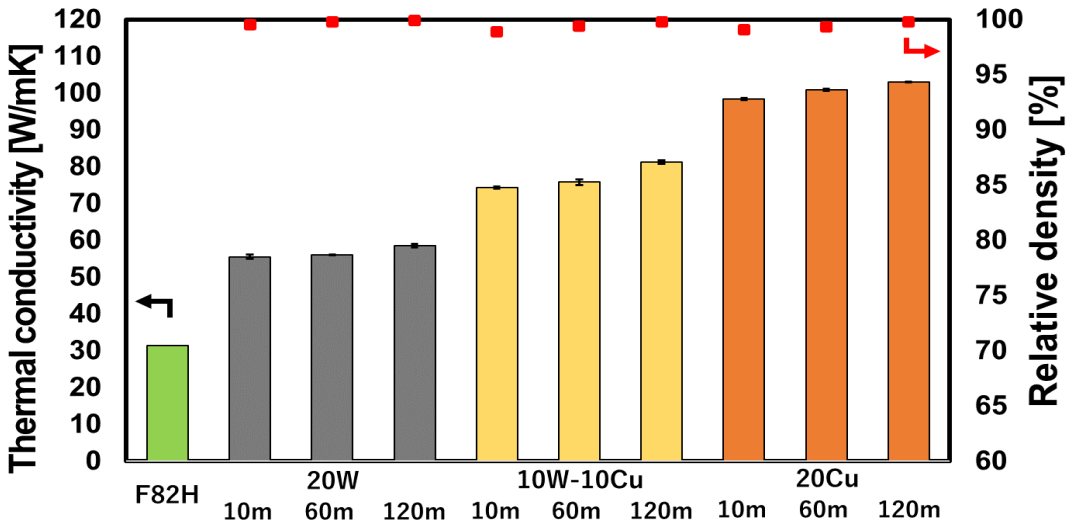

Figure 3.2 Thermal conductivities and relative densities of F82H-xW-yCu composites under diverse SPS conditions at 1000 °C

	SPS Holding Time [min]	Expected thermal conductivity [W/(m•k)]	Actual thermal conductivity [W/(m•k)]	Relative density [%]
F82H Bulk [8]	-	-	**31.3**	**100**
20W	10	59.8	55.5	99.5
20W	60	59.8	56.0	99.8
20W	**120**	**59.8**	**58.5**	**99.9**
10W-10Cu	10	82.5	74.4	98.9
10W-10Cu	60	82.5	75.7	99.4
10W-10Cu	**120**	**82.5**	**81.2**	**99.8**
20Cu	10	105.2	98.3	99.1
20Cu	60	105.2	100.9	99.3
20Cu	**120**	**105.2**	**103.0**	**99.8**

Table 3.2 Thermal conductivities and relative densities of composite materials SPSed at 1000 °C

3.3 Microstructure of F82H-based composite materials

3.3.1 Microstructure of F82H-based composite materials SPSed at 850 °C

Microstructure of F82H-xW-yCu composites was investigated by using SEM and EDS. Figure 3.3 shows SEM images of 15W-5Cu composite SPSed at 850 ℃ for 10 min SPS holding. These figures were taken in *x*-axis, thus both W and Cu wires are circular shape. The gray-colored areas show Cu wire and bright silver-colored areas are W wire. At the F82H matrix, many pores were observed around wires. It may occur the decrease in the density and mechanical properties.

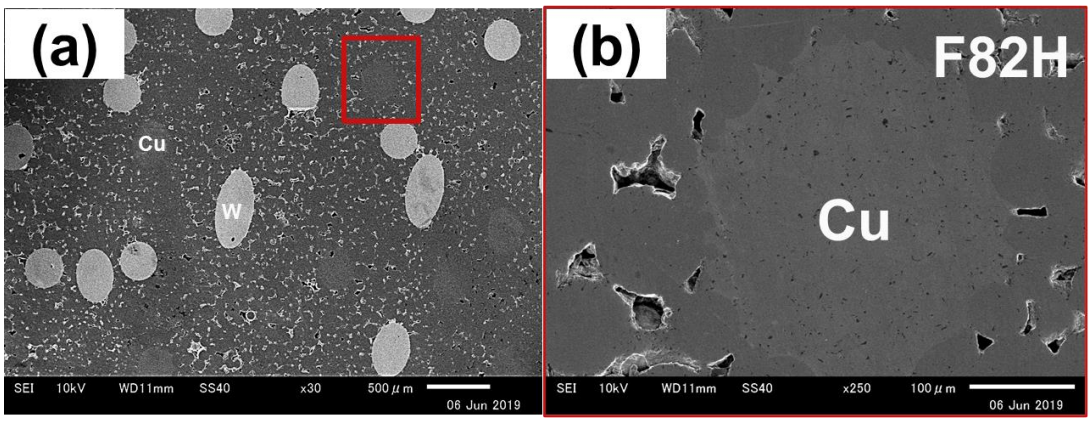

Figure 3.3 (a) surface of 15W-5Cu composite SPSed at 850 ℃ for 10 min and (b) Cu wire surrounded by F82H matrix and pores

For the 15W-5Cu and 5W-15Cu composites, the pores in the F82H matrix did not disappear even after sintering at 850 ℃ for 120 min, as shown in figure 3.4. The copper wire was deformed from a circular shape to a flake shape due to a pressure of 40 MPa applied for a long time.

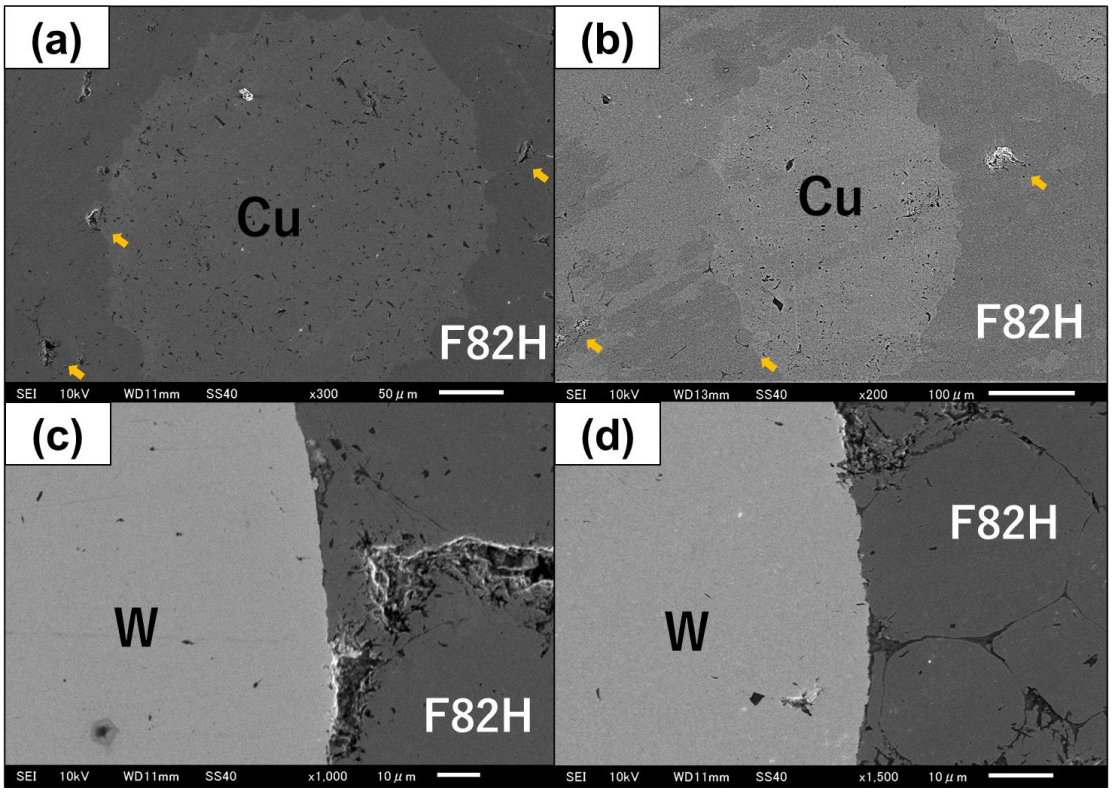

Figure 3.4 Surface of (a), (c) 15W-5Cu and (b), (d) 5W-15Cu composites SPSed at 850 ℃ for 120 min

3.3.2 Microstructure of F82H-based composite materials SPSed at 1000 °C

Fig. 4.3(a)–(i) show surface structures of F82H-20Cu, F82H-10W-10Cu and F82H-20W composites SPSed at 1000 ℃ for 10 to 120 min. As an aspect of the SPS holding time, the thermal conductivity of each specimen increases with its relative density. Cu wires became softer and were shaped like flakes under the high pressure of 40 MPa for the longer sintering time. As indicated by arrows in Fig. 3.5(a), (d) and (g), the diverse and multitudinous pores were formed in F82H matrix. For 10 min SPS holding time, F82H powder with a spherical shape could be observed probably because of its not enough SPS holding time. As shown in Fig. 3.5(a)-(c), (d)-(f), and (g)-(i), increase the SPS holding time tends to decrease the number of pores. For example, with 60 min holding time, the number of pores has decreased compared to that of 10 min holding time. The pores finally disappeared in the SPS condition for 120 minutes. In figure 3.6, ferritic/martensitic microstructure with precipitates ($M_{23}C_6$, MX) were observed in F82H matrix after SPS at 1000 ℃. It appears that no microstructure modification occurred from tempered ferritic/martensitic structure to ferritic structure with the thermal profile which is SPS at the temperature of 1000 ℃ for 120 min and the annealing at a temperature of 800 ℃ for 180 min.

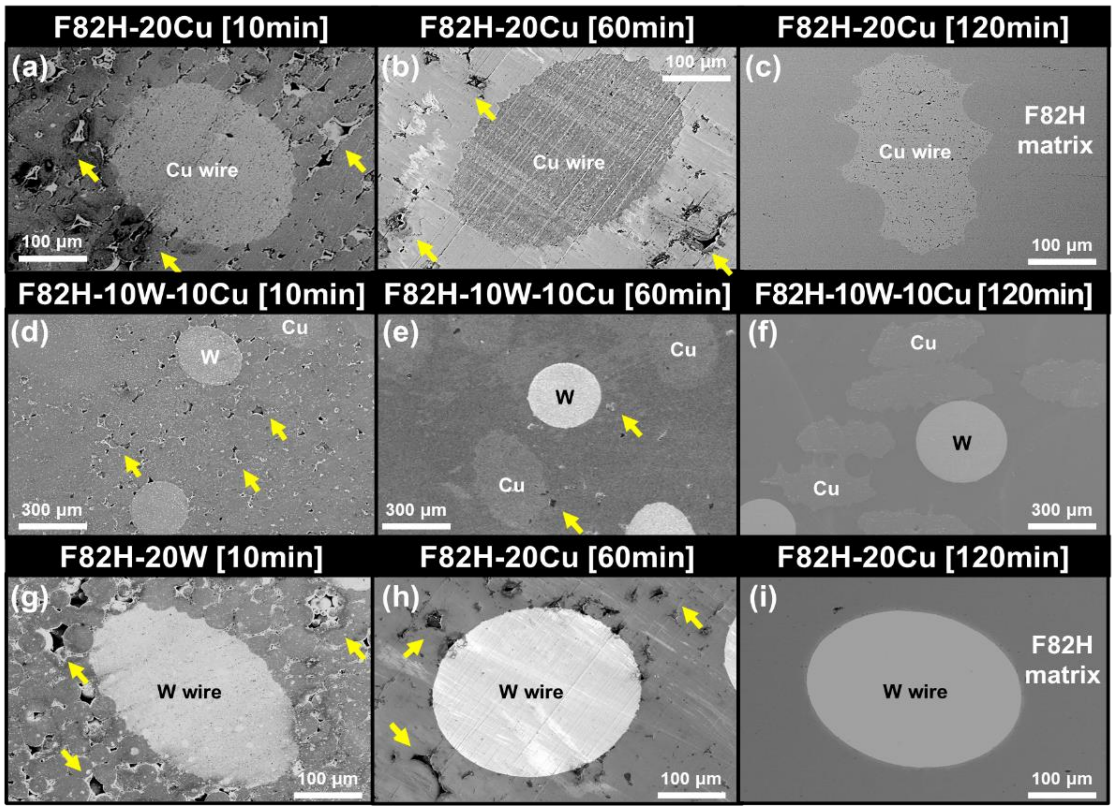

Figure 3.5 Cross-sectional SEM images of F82H-20Cu, F82H-10W-10Cu and F82H-20W composites with 10 to 120 min SPS holding time

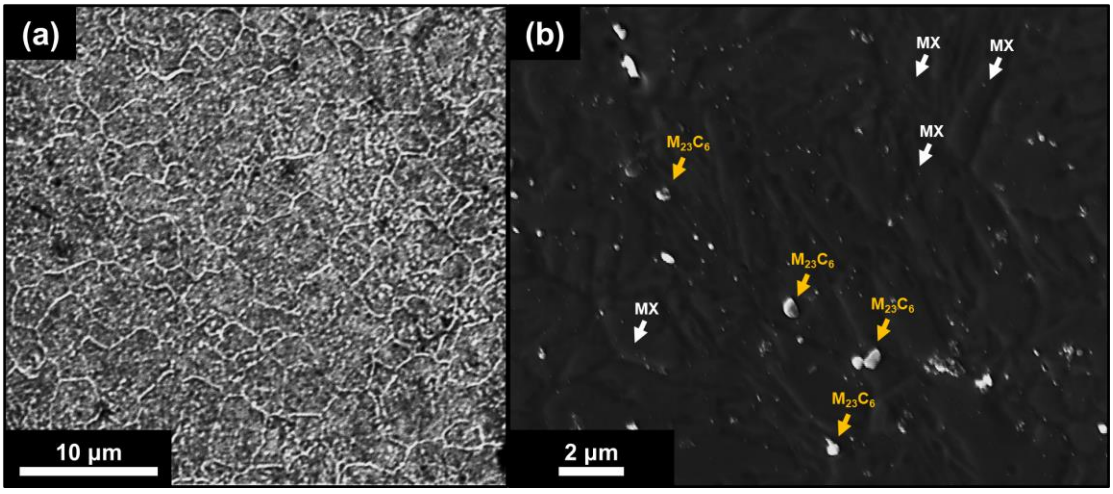

Figure 3.6 Surface of electro-polished F82H part in F82H-20W composite material

However, the reaction layer formed at the interface between F82H and W. As shown in Fig. 3.7, the average thickness of F82H-W reaction layer in F82H-20W SPSed at 1000 °C for 10 min, 60 min and 120 min is 0.85 μm, 1.30 μm and 1.42 μm, respectively. The thickness of reaction layer is increase with SPS holding time. The F82H-W reaction layer, the intermetallic compound consists of Fe_7W_6 μ-phase and Fe_2W laves phase. It makes the composite material harder with an extremely high brittleness due to its very high hardness.

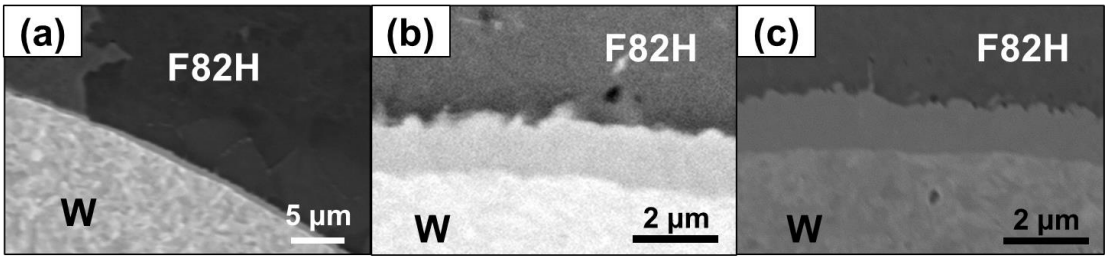

Figure 3.7 The reaction layer at the interface between F82H and W

3.4 Tensile property of F82H-based composite materials

Stress-strain curves of F82H-15W-5Cu, F82H-10W-10Cu and F82H-5W-15Cu are plotted in figure 3.8. The deterioration of the physical properties of the F82H composite material revealed in the Vickers hardness test is also shown in the tensile test. Entire yield strengths, ultimate tensile strengths (UTS), total elongation and toughness of F82H-based composite materials reduced after SPS with holding at 850 °C. As a result, the F82H-based composite material under the sintering condition of 850 °C holding temperature shows about 10 times lower yield strength and elongation than F82H sintered using only F82H powder, as shown in figure 3.8 (a).

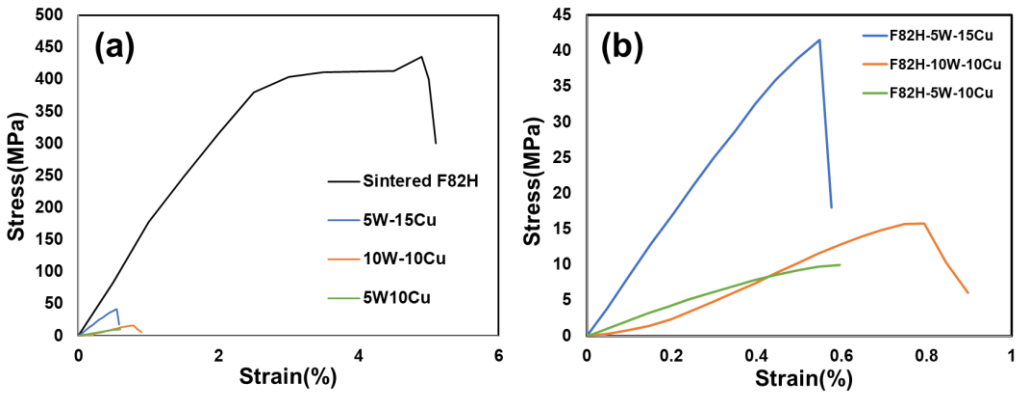

Figure 3.8 stress–strain curves of sintered F82H, F82H-5W-15Cu, F82H-10W-10Cu and F82H-5W-10Cu composites

Fig. 3.9 (upper left) shows the cross-sectional SEM micrograph of F82H-10W-10Cu

composite. The EDS mapping showed the reaction layers and the diffusion layers between F82H matrix and W wire in the F82H-5W-15Cu composite as shown in figure 3.9. From the observation of the fracture surface, it can be seen that the raw material, F82H powder maintains a spherical shape, and the produced composite material lacks sinterability.

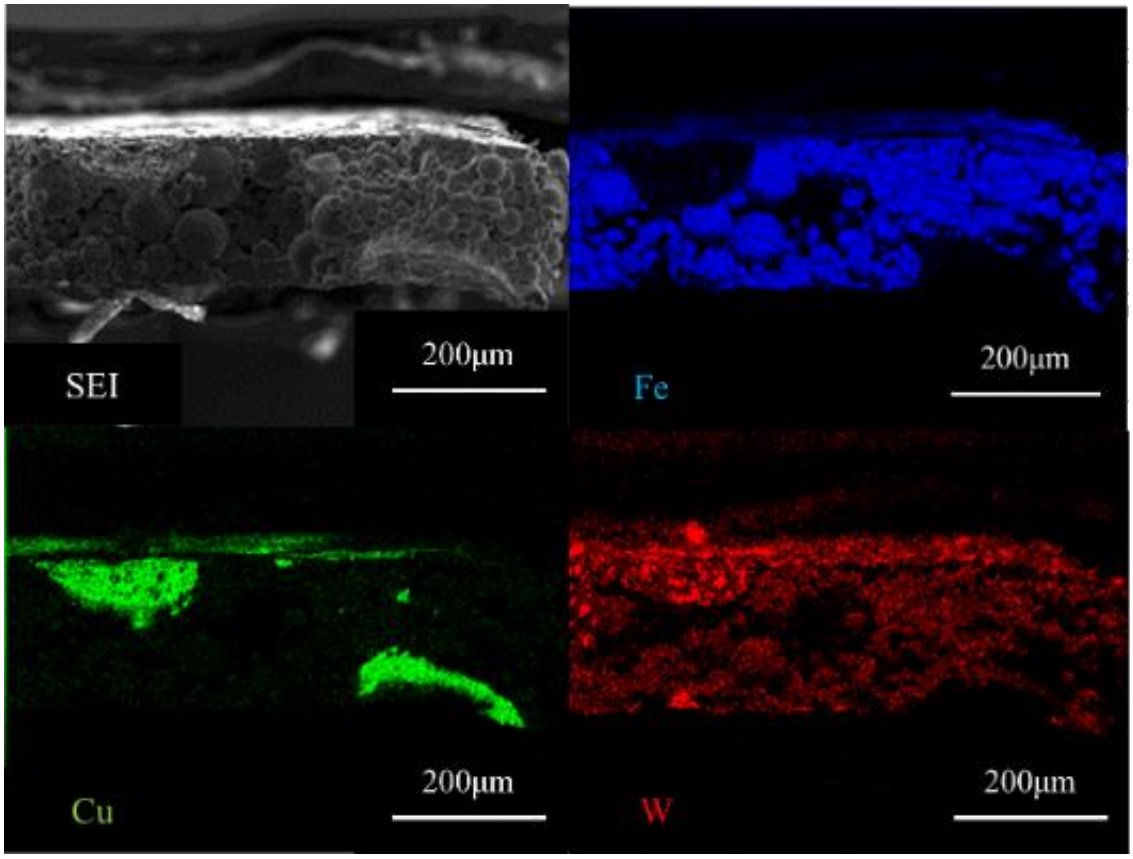

Figure 3.9 SEM image and EDS mapping images at the fracture surface of the F82H-5W-15Cu after tensile test

The engineering stress-strain curves of the composites are presented in figure 3.10. The 0.2 % offset yield stress, ultimate tensile strength and total elongation of the composite materials are listed in Table 3.3. All the tensile-tested specimens had failed in the mid-substance. F82H-20W composite material SPSed at 1000 ℃ for 120 min shows the highest ultimate tensile stress of 605.9 MPa among all composite materials. In contrast, F82H-20Cu

composite material SPSed at 1000 ℃ for 120 min shows the highest engineering strain with the total elongation of 17.7 %, which statistically greater than F82H-20W and F82H-10W-10Cu composite material.

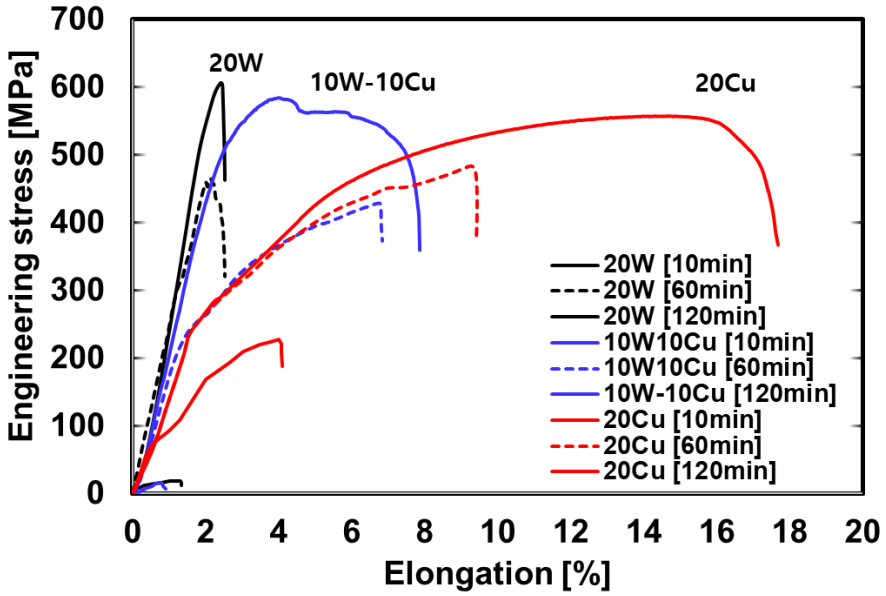

Figure 3.10 Engineering stress-strain curves on F82H-based composites SPSed at the temperature of 1000 °C

ID [SPS holding time]	0.2% offset yield stress (Mpa)	Ultimate Strength (Mpa)	Total Elongation (%)
F82H[8]	548	669	21.7
20W [10 min]	7.2	18.3	1.3
20W [60 min]	497.6	464.0	2.4
20W [120 min]	514.4	605.9	2.5
10W-10Cu [10 min]	8.4	16.0	1.0
10W-10Cu [60 min]	384.3	428.9	6.8
10W-10Cu [120 min]	479.5	583.6	8.0
20Cu [10 min]	112.6	226.6	4.1
20Cu [60 min]	422.8	482.9	9.4
20Cu [120 min]	439.2	556.6	17.7

Table 3.3 Tensile properties of composite materials SPSed at 1000 °C

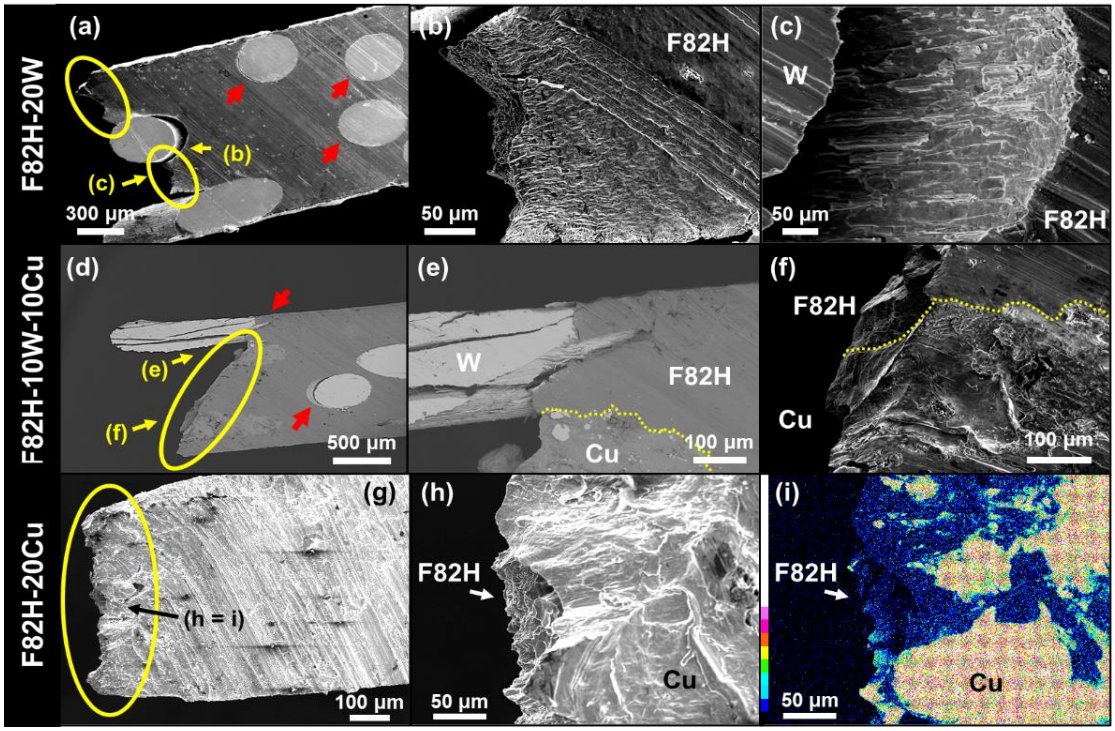

Figure 3.11 SEM images and EDS mapping data of fracture surfaces on F82H-20W (a–c), F82H-10W-10Cu (d–f) and F82H-20Cu (g–h) composites with 120 min SPS holding time

In order to carry out the investigation of the fracture mode on the composite materials, SEM observation was performed on the failed area of the tensile-tested specimens. Fig. 3.11(a)–(c), 3.11(d)–(f), and 3.11(g)–(h) show SEM images of the edge of the tensile-tested F82H-20W, F82H-10W-10Cu, and F82H-20Cu composite materials with the SPS condition of 120 min holding time, respectively. As shown in the SEM images, it is recognized that F82H-20W and F82H-10W-10Cu were deformed with phase separation at the interface between W-wire and F82H matrix. In contrast, F82H-20Cu composite material showed no phase separation but the deformation with necking. While the fracture surface of F82H area

showed dimple structure as shown with yellow circles in Fig. 3.11(a), 3.11(d) and 3.11(g). As shown in figure 3.11 (i), The EDS mapping performed for the tip of the tensile-tested F82H-20Cu composite material indicated that the interface between copper-wire and F82H matrix would be stable even after the deformation.

3.5 Summary

The objective of this chapter is the optimization of the SPS condition and the value of (x, y) in F82H-xW-yCu composites on a basis of the higher thermal conductivity. First, F82H-15W-5Cu, F82H-10W-10Cu and F82H-5W-15Cu were fabricated at SPS holding temperature of 850 °C for 10 min, 60 min and 120 min in order to find a proper with high thermal conductivity. From the observation of the fracture surface, it can be seen that the raw material, F82H powder maintains a spherical shape, and the produced composite material lacks sinterability. Relative density also shows a low tendency with 98 % or less value due to sintering with low completeness. Since the low relative density acts as a fatal factor for lowering the tensile strength of the composite material, improvement of sinterability is required. In order to compress the composite materials by increasing the relative density, sintering at a higher temperature is required for a long time. It is necessary to find a stable SPS condition at a temperature as high as possible in a temperature range lower than the melting point of copper wire.

As listed in Table 4.1, the composite material, including larger volume fraction of copper, shows higher thermal conductivity than tungsten-rich composite materials. Under these results, the amount of copper wire could show more effective improvement for the increase in the thermal conductivity than tungsten wire. Therefore, in the aspect of thermal conductivity, the best content fraction of the composite material with the highest thermal conductivity and mechanical property would be F82H-20W in this chapter. The formation of pores in sintered materials is a very critical issue because it would degrade the thermal conductivity and the tensile property due to the decrease in relative density. Actually, in this study, the decrease in relative density resulted in the decrease in thermal conductivity. According to SEM observation, the number of pores in sintered composites was decreased

with longer holding time. The SPS for 120 min resulted in no formation of a pore in F82H matrix with 99% or higher relative densities. Hence, a longer SPS holding time (> 120 min) would be effective to make F82H-20Cu composite a denser and a higher thermal conductivity material. In addition, the interface between tungsten-, copper wire and F82H would act an important role to its tensile property total elongation (TE), 0.2 % offset yield stress, and the ultimate tensile strength (UTS) of the general F82H steel are 21.7 %, 548 MPa and 669 MPa, respectively. However, the sintered composites resulted in the decrease in the tensile properties compared to general F82H. In terms of F82H-20W composite with 120 min SPS holding time, the 0.2 % proof stress and the UTS were the highest, while the TE was the worst among all composite materials with 1000 ℃ SPS holding temperature. The separation of tungsten wire from F82H matrix was observed in F82H-20W and F82H-10W-10Cu composite materials due to the formation of the reaction layer or intermetallic compounds at the interface between tungsten wire and F82H during sintering. It was reported that the reaction layer and the diffusion layer in F82H-W wire composite material [3]. Basically, tungsten and ferritic steel have differences in their coefficients of thermal expansion, melting temperature, and elasticity modulus [4-5], so that the rapid temperature change would generate high internal stresses, leading to separation or failure [6]. In addition, it was reported that the formation of intermetallic compounds such as Fe_7W_6, Fe_3W_3C and Fe_2W phases could be found between tungsten and matrix in sintered steels [7]. Following our previous report [3], the formation of Fe_2W and Fe_7W_6 intermetallic compounds would occur in this study. The formation of intermetallic compounds at the interface between matrix and W wires would reduce the mechanical property of the sintered composites because it could be a source of crack initiation during deformation. In actual, those tungsten wires in F82H-20W and F82H-10W-10Cu were pulled out from the F82H matrix during tensile testing as shown in Fig. 6. In contrast, F82H-20Cu composite material showed no separation or crack initiation

at the interface between F82H and copper wire, resulted in a satisfactory tensile property. From those results, F82H-20Cu composite material SPSed at 1000 ºC for 120 min is suggested that the optimized condition to improve the thermal conductivity, leading to a comparable tensile property with that of the original F82H.

References

[1] SCHUH, Christopher A. Nanoindentation studies of materials. Materials today, 2006, 9.5: 32-40.

[2] PIETRAK, Karol; WISNIEWSKI, Tomasz S. A review of models for effective thermal conductivity of composite materials. Journal of Power Technologies, 2015, 95.1: 14.

[3] PROGELHOF, R. C.; THRONE, J. L.; RUETSCH, R. R. Methods for predicting the thermal conductivity of composite systems: a review. Polymer Engineering & Science, 1976, 16.9: 615-625.

[4] HEO, Jeongwoo, et al. Improvement of thermal conductivity by adding tungsten and/or copper wire in F82H. Journal of Nuclear Science and Technology, 2021, 1-6.

[5] NIX, F. C.; MACNAIR, D. The thermal expansion of pure metals. II: molybdenum, palladium, silver, tantalum, tungsten, platinum, and lead. Physical Review, 1942, 61.1-2: 74.

[6] TAVASSOLI, A.-AF, et al. Materials design data for reduced activation martensitic steel type F82H. Fusion Engineering and Design, 2002, 61: 617-628.

[7] ÇAM, Gürel; KOÇAK, Mustafa. Progress in joining of advanced materials. International Materials Reviews, 1998, 43.1: 1-44.

[8] Shiba K, Hishinuma A, Tohyama A, Masamura K. Properties of low activation ferritic steel F82H IEA heat. Japan: Japan Atomic Energy Research Institute; 1997. (Report JAERI-Tech 97-038)

Chapter 4

Microstructure analysis in irradiated RAFM and F82H composite materials

4.1 Introduction

In the previous chapter, various F82H-xCu-yW (x, y = 0~20 vol.%) composite materials had been fabricated with copper wires and/or tungsten wires (401 W/(m•K) of pure Cu and 173 W/(m•K) of pure W) to improve the thermal conductivity by using the spark plasma sintering (SPS). The thermal conductivity of F82H could be increased three times higher by adding 20 vol.% of Cu wires with F82H. In F82H-20Cu composite material shows 3.3 times higher (103 W/(m•K)) thermal conductivity than general F82H (31.3 W/(m•K)) with satisfactory mechanical properties. However, the results were investigated under the atmosphere with no radiation source at the room temperature. As the result, the swelling resistance and irradiation hardening effect on F82H-based composite materials are not included in the previous chapter. During the operation of a nuclear fusion reactor, heavy hydrogen isotopes (Deuterium and Tritium) will be used as fuel, hostile conditions generating a high flux of neutrons with high heat loads for plasma facing components (PFCs) will be created during the fuel synthesis. The structural material for DEMO reactor needs long lifetime and stability based on good thermal and mechanical properties for harsh operating condition. Therefore, the evaluations of irradiation resistance on irradiation hardening and helium embrittlement are required for the F82H-based composite material. In this study, swelling and the irradiation hardening behaviors in triple ion beam (Fe^{3+}, He^{+} and H^{+}) irradiation on F82H-based composite materials were investigated by transmission electron microscope (TEM) observation and the nano-indentation test. To compare the difference in microstructures with irradiation condition, ion irradiation for Fe^{3+} ion beam, and He^{+} gas implantation was performed to two reference RAFM steels, respectively. And the hardness change by the irradiation hardening was analyzed by using Nix-Gao model for F82H-based composite materials [1-3]. Nano-indentation tests were carried out to measure nano-scale

hardness on ion-irradiated composite materials. For the nano-indentation test on the composite material, the major controversy is that the hardness of the measured object varies depending on the kinds of material. The Fe contained in F82H and the tungsten wire react to form Fe_7W_6 μ-phase and Fe_2W λ-phase [4-7]. In particular, the investigation for the irradiation hardening on the F82H-W reaction layer surrounding surface of W wire, Fe_7W_6 μ-phase intermetallic compound with a size of several micrometers is important [4]. In addition, the microstructural understanding should be investigated as well as the thermal conductivity for the PFMs in order to clarify the characterization of the irradiation effect on the composites after the irradiation.

4.2 Microstructure analysis for irradiated RAFM

To compare the difference in microstructures with irradiation condition, between SPSed composite material and general RAFM steel, two kinds of reference RAFM steels were fabricated. The chemical compositions of RAFM steels are listed in table 4.1. As shown in table 4.2, ion irradiation for Fe^{3+} ion beam and He^{+} gas implantation was performed to RAFM steels, respectively. And then, analysis of radiation damage distribution was performed for Fe^{3+} ion beam irradiated specimens. Cavity distribution and swelling were analyzed for the He^{+} gas implanted specimens. The surface structures of RAFM steels are presented in Fig. 4.1.

	Cr	W	V	Ta	Mn	Ti	C	Si
RAFM 1	9.3	0.93	0.22	0.094	0.40	-	0.10	0.11
RAFM 2	9.1	1.1	0.21	0.1	0.42	0.015	0.10	0.11

Table 4.1 Chemical compositions of reference RAFM steels

Ion species	Temperature	Maximum dpa	Ion concentration
Fe^{3+}	325 °C	~6 dpa	self-ion
He^{+}	R.T. ➔ Annealing @350°C for 2hr	0.45 dpa	11000 appm

Table 4.2 Ion irradiation conditions for reference RAFM steels

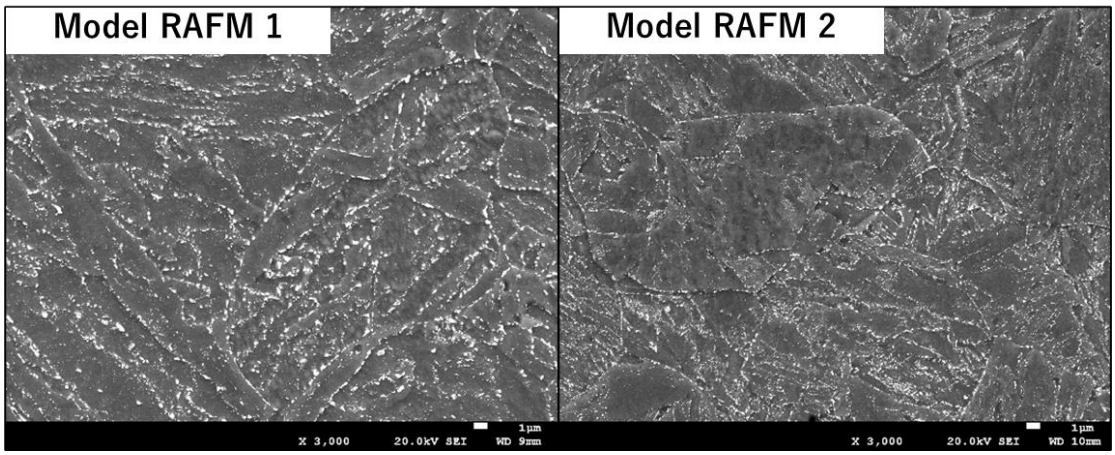

Figure 4.1 Surface structures of RAFM steels used in this chapter

The depth profile of displacement damage for 6.4 MeV Fe^{3+} ions is presented in figure 4.2. Heavy ion irradiation was performed on both steels using the DuET (Dual-Beam Facility for Energy Science and Technology) facility at Kyoto University. $Fe3^{+}$ ions were used as the irradiated ion species and irradiated at an average temperature of 325 °C with an energy of 6.4 MeV. As a result of stopping and range of ions in matter (SRIM) simulation, it was found that the maximum dpa with irradiation damage was 5.8 dpa at a depth of about 1.5 um from the surface of specimens [8-9].

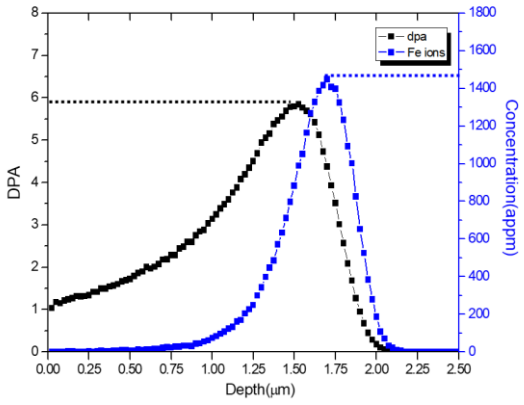

Figure 4.2 SRIM prediction profile for depth distribution of displacement damage for 6.4 MeV Fe^{3+} ions

The microstructures in ion-irradiated RAFM are presented in figure 4.3 with bright-field (BF) TEM image. Fig. 4.3 (a) and (d) show the low-magnification TEM images of the irradiated RAFM steels. As shown in figure 4.3 (c) and (f), there are few dislocation loops with 'coffee bean' shape at the shallow area of 500 nm depths.

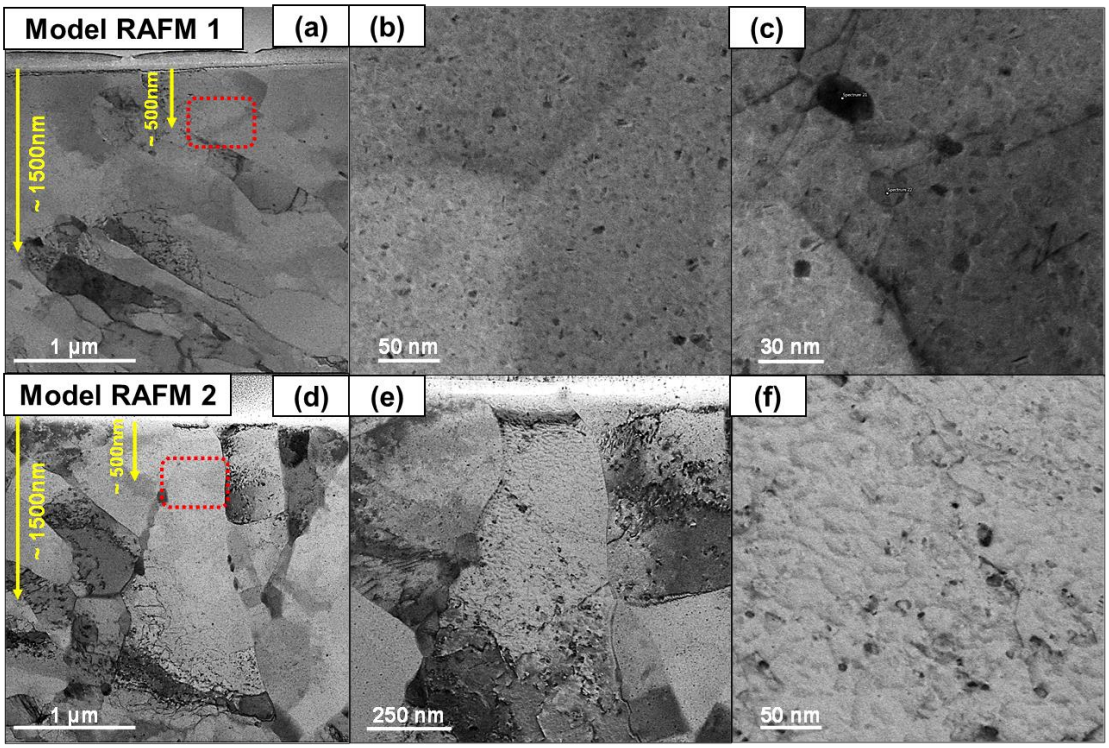

Figure 4.3 Microstructures in Fe^{3+} ion irradiated RAFM steels

In the depth of damage peak at 1500 nm, microstructures with the weak beam dark-field (WBDF) TEM images are presented in figure 4.4. The major proportion of dislocation loops with a_0<100> loop-type and a small proportion of $a_0/2$<111> type burgers vectors are indicated by white solid and dashed arrows, respectively. Analyzed mean diameter and number density of dislocation loops are listed in table 4.3.

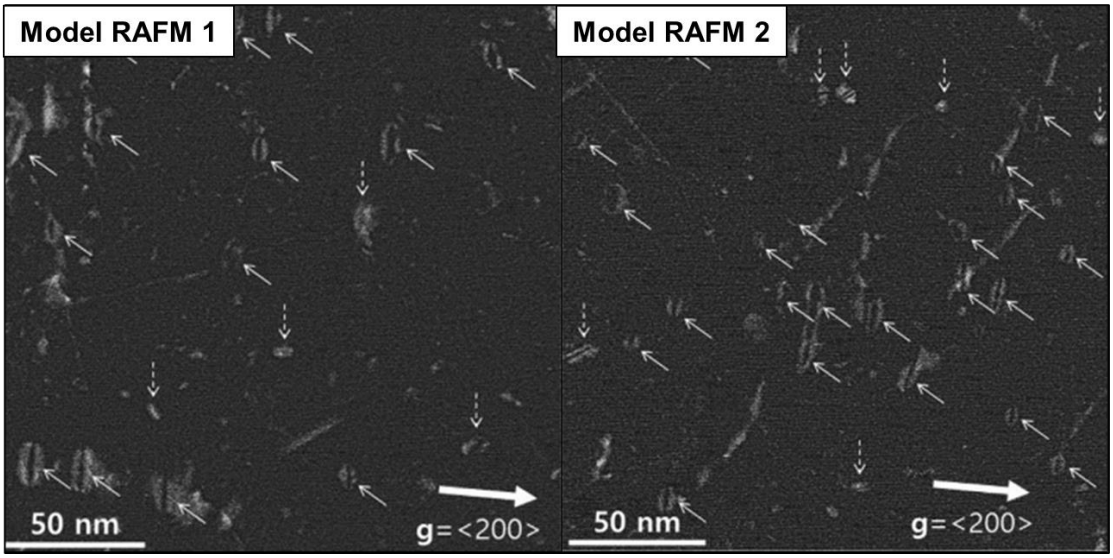

Figure 4.4 Weak beam dark-field TEM micrographs of microstructures in Fe^{3+} ion irradiated RAFM steels

	Mean loop diameter (nm)	Dislocation loop density (10^{21} m^3)
Model RAFM 1	**12.6 ± 4.5**	**7.1 ± 1.5**
Model RAFM 2	**14.3 ± 5.7**	**4.9 ± 1.8**

Table 4.3 Mean dislocation loop diameter and density in RAFM steels irradiated at 325 °C

Ion beam irradiation-induced dislocation loop distributions in irradiated RAFM steels are given in figure 4.5. The mean loop diameter is slightly higher, and the number density is lower for the model RAFM 2 compared to those for the RAFM 1. However, the differences in loop diameter and number density of the two RAFM steels are not significant.

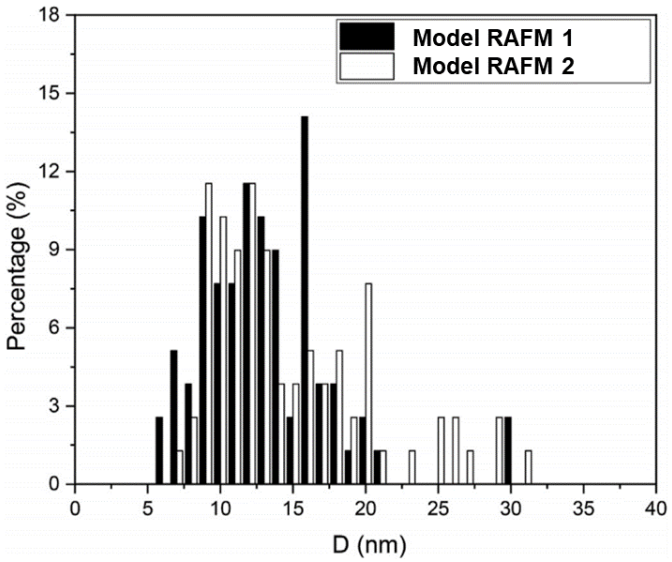

Figure 4.5 Dislocation loop distribution in ion-irradiated RAFM steels

He ion implantation performed with a max He concentration of 11000 appm at 550 nm depths as shown in figure 4.6. The RAFM steels were implanted at the room temperature, and then annealed at 350 ℃ for 2 hours in the vacuum furnace.

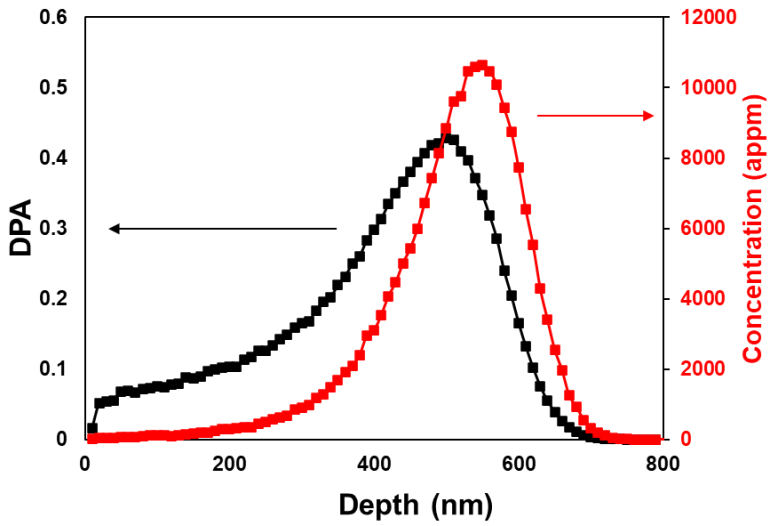

Figure 4.6 Dislocation loop distribution in ion-irradiated RAFM steels

After He implantation, no dislocation loop but large number of He bubbles with small sizes have been observed at 550 nm depths. As shown in figure 4.7, grain and lath boundaries could be trap sites for vacancy. The number density and average size of cavities formed in

He implanted RAFM steels were listed in table 4.4. A higher number density (10^{24} m^{-3}) and similar diameter (~1.5 nm) of bubbles were formed with a high concentration of He^{+} gas. Average size and number density of cavities and swelling fraction in RAFM 1 is slightly larger than RAFM 2.

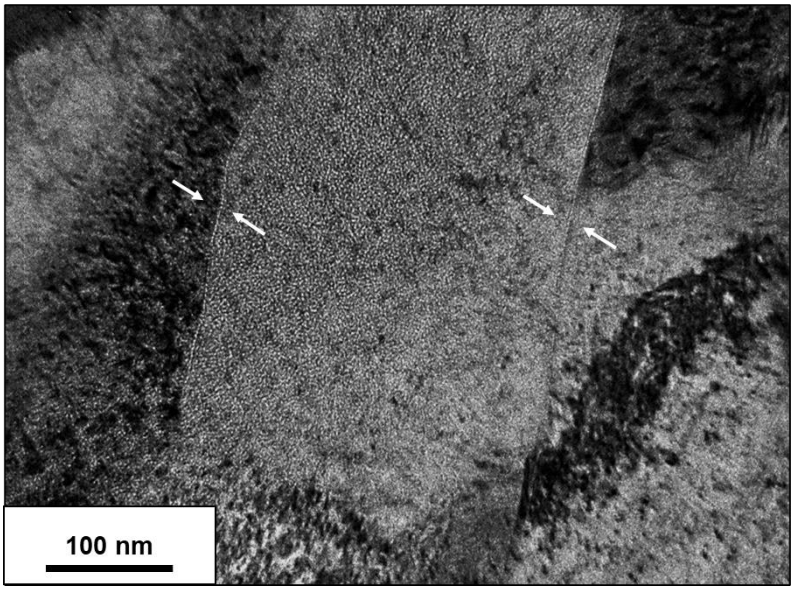

Figure 4.7 Dislocation loop distribution in ion-irradiated RAFM steels

	Mean diameter (nm)	Number density (10^{23} m^{-3})	Swelling
Model RAFM 1	**1.68**	**6.7 ± 1.2**	**2.87 %**
Model RAFM 2	**1.32**	**6.3 ± 1.8**	**2.62 %**

Table 4.4 Mean cavity diameter, number density and swelling fraction in He implanted RAFM steels

4.3 Microstructure analysis for irradiated F82H composite materials

Each specimen of F82H composites was irradiated by triple beam (0.38 MeV H^+ with 40 appm/dpa, 1.05 MeV He^+ with 15 appm/dpa and 10.5 MeV Fe ion with 20 dpa at 1μm) at an average temperature of 350°C or 500 ℃ at TIARA (Takasaki Ion Accelerators for Advanced Radiation Application) facility in National Institutes for Quantum Science and Technology (QST). During the irradiation, the energy degraders in the accelerator were applied to make a flat ion-concentration peak for He^+ and H^+ irradiation. The depth profile of ion-induced damage distribution was calculated by using the SRIM simulation software. SRIM is a Monte Carlo simulation code widely used to calculate process parameters related to ion implantation and ion irradiation processes in various materials [10]. Using SRIM code, the amount of radiation damage caused by ion irradiation, displacements per atom (DPA) calculated for irradiated F82H-based composite materials. Since DPA is widely used as a standard unit for initial irradiation damage in irradiation damage, it is necessary to simulate the irradiation damage with a depth profile by SRIM for researchers using an ion beam as a source of irradiation damage. The displacement energy of atoms for the F82H-based composite material was set to 40 eV [11]. This value is recommended by ASTM for polycrystalline materials [12]. As shown in figure 4.8, SRIM prediction profile of depth distribution of displacement damage for 10.5 MeV Fe^{3+} ions (Blue) and implanted ions for 1.05 MeV He^+ ions and 0.38 MeV H^+ ions (Red) irradiated to F82H substrate were presented. In the case of He^+ and H^+ ions, the irradiated layer has a thickness of about 2 μm. The contribution of helium to the total displacement damage is less than 0.01 DPA. Thus, the ion concentration according to the depth was plotted to investigate the hardening of the material due to implantation inside the base materials.

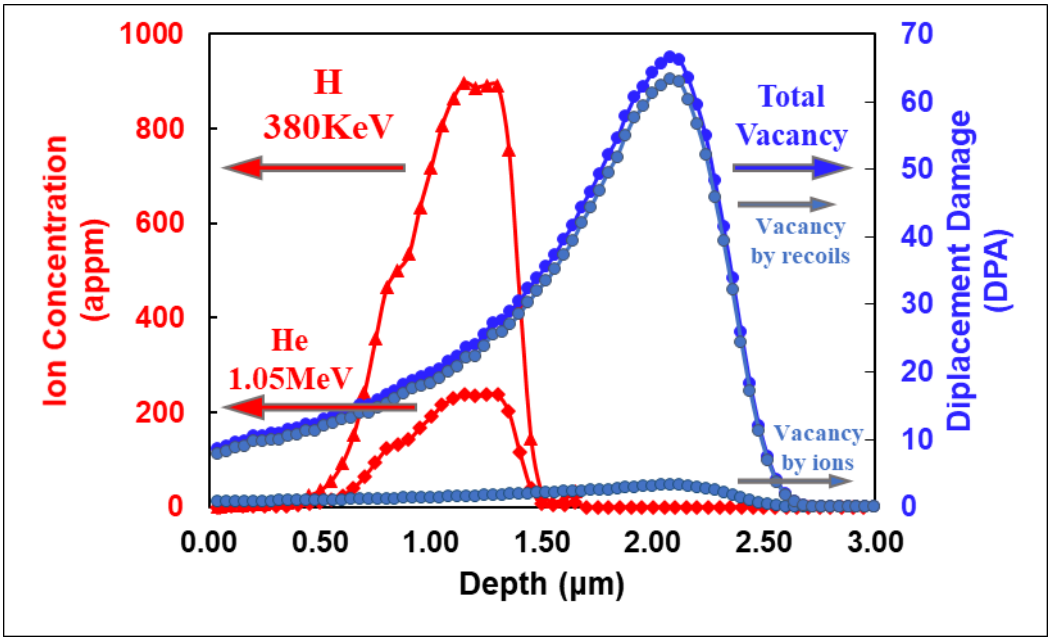

Figure 4.8 SRIM prediction profile of depth distribution of displacement damage for 10.5 MeV Fe3+ ions (Blue) and implanted ions for 1.05 MeV He+ ions and 0.38 MeV H+ ions (Red)

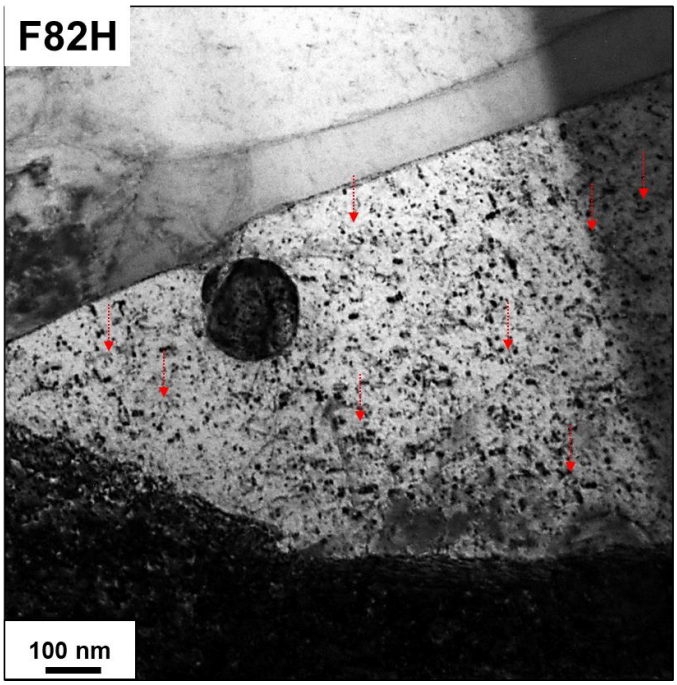

Figure 4.9 Dislocation loops with 'coffee bean' contrast at 1600 nm depths in F82H irradiation at 350 °C

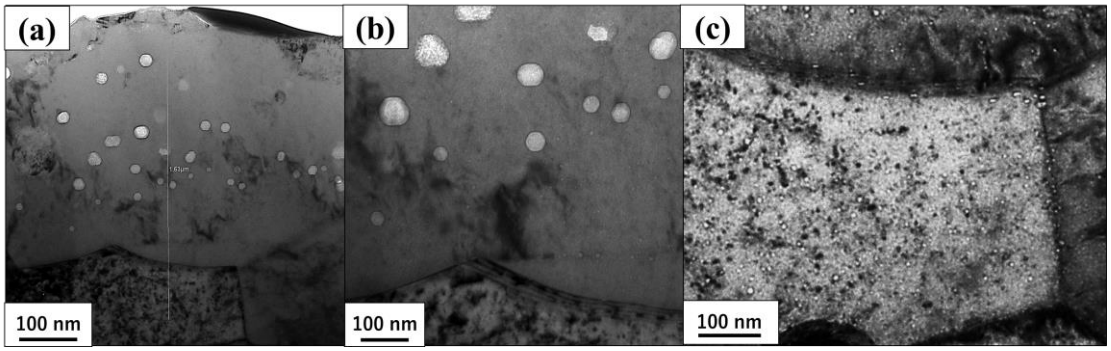

Figure 4.10 (a) The low-magnification TEM micrograph and high-magnification microstructure at (b) 800 nm and (c) 1600 depths in F82H irradiation at 350 °C

As shown in figure 4.9, 'Coffee-bean' shaped dislocation loops were observed at 1600 nm depths in F82H irradiation at 350 °C. And, TEM analysis of the defects generated by Ga^{+}

ions damage at the same grain revealed the presence of dislocation and black spot damage. No significant differences between ion beam irradiation-induced damage and Ga^+ FIB generated defect microstructures were observed. In figure 4.10 (a), the low-magnification TEM micrograph for the observation of entire was given. As presented in figure 4.10 (b), large voids mainly exist in shallow area of 800 nm depths Huge voids were formed from the area shallower than 800 nm depth. The voids were getting smaller and small bubbles were formed from 600 nm to 1600 nm depths. A large amount of small size (1~10 nm diameters) He bubbles were observed in deep area of 1600 depths. Mean diameter and number density of cavities, and swelling fraction of F82H part were listed in F82H-based composite material irradiated at 350 °C as shown in table 4.5.

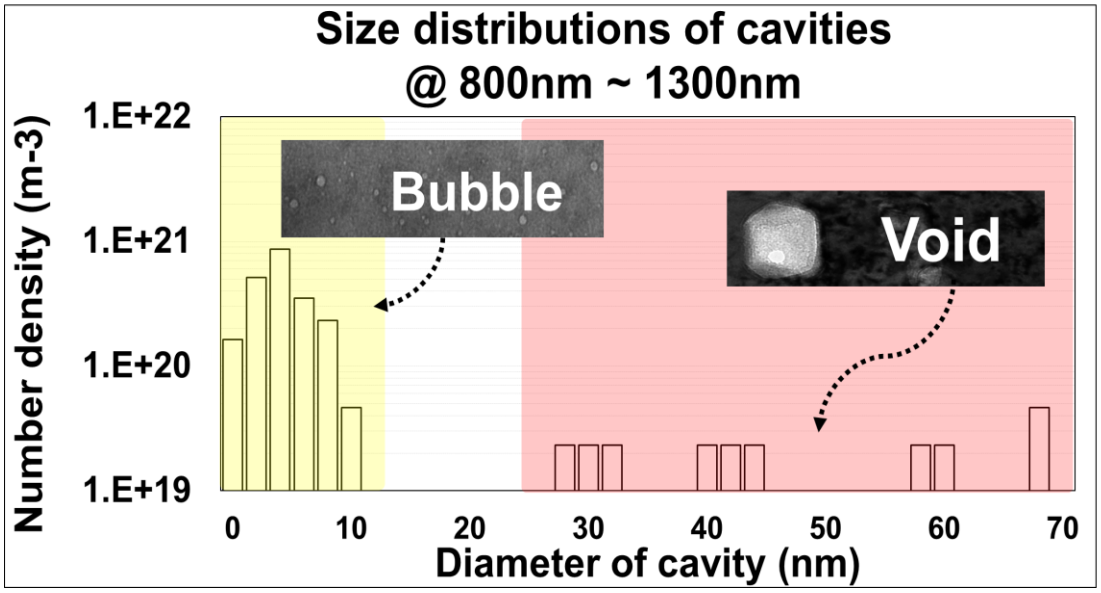

Figure 4.11 Dislocation loops with 'coffee bean' contrast at 1600 nm depths in F82H irradiation at 350 °C

number density (m^{-3})	Cavity diameter	Swelling (%)

	(RMC)	
9.1×10^{20}	23.0 nm	4.6 %

Table 4.5 Mean cavity diameter, number density and swelling fraction in F82H composites irradiated at 350 °C

Focused ion beam (FIB, Hitachi, FB-2100) milling to the interface between F82H and the additives was performed to fabricate specimens for each F82H-20W and F82H-20Cu composite material which were irradiated for triple ions at 500 °C as shown in figure 4.12. The FIB milling generated cross-section TEM specimens perpendicular to the direction of irradiated surface. FIB-milled TEM specimen of F82H-W or F82H-Cu is including F82H, W and Cu, respectively. The thickness of the TEM specimens was from 70 to 80 nm. For the microstructure observation, transmission electron microscopy (TEM, JEOL, JEM-2010) was performed at 200 kV.

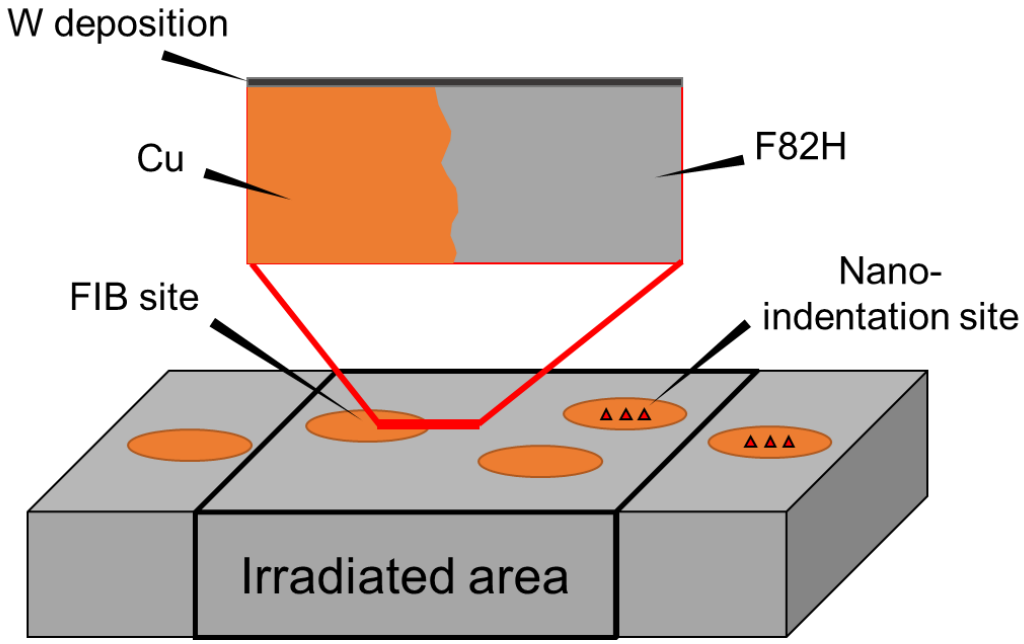

Figure 4.12 conceptional image of the specimen preparation by using FIB

The bright-field (BF) TEM images are presented in Fig. 4.13 and Fig. 4.14. Under-

focused BF-TEM images of irradiated F82H-based composite materials are shown in Fig. 4.13 (b) and Fig. 4.14 (b)-(c). In F82H part of both composite materials, He-induced bubbles and voids were observed at the depth of the He concentration peak in F82H. The voids have the size of about 30 nm or larger in diameter and have a hexagonal shape. He bubbles have a circular shape of several nanometers in diameter. As shown in Fig. 4.15, the microstructure observation showed that irradiation-induced small-size He bubbles (<12 nm) were formed in the F82H-W reaction layer part of the F82H-20W composite material. The large amount of He bubbles, and a few voids were observed at the reaction layer part in F82H-20W composite. In contrast, there was no bubble or void in W wire part of F82H-20W composite and Cu wire part of F82H-20Cu composite. For the specific comparison, statistical size distributions were investigated with various sizes of cavities, as shown in figure 4.16. The cavities were divided into bubbles and voids in size and shape on F82H areas and the F82H-W reaction layer in F82H-W and F82H-Cu composite materials. The number density and diameter of root mean cube of cavities formed in F82H-based composite materials irradiated by triple ion-beam are listed in Table. 4.6. Compared with the irradiated materials, in the F82H-W reaction layer, higher density of He bubbles was formed than in F82H. Overall swelling fraction in the reaction layer was smaller than F82H due to the He Bubbles of much smaller size than the voids.

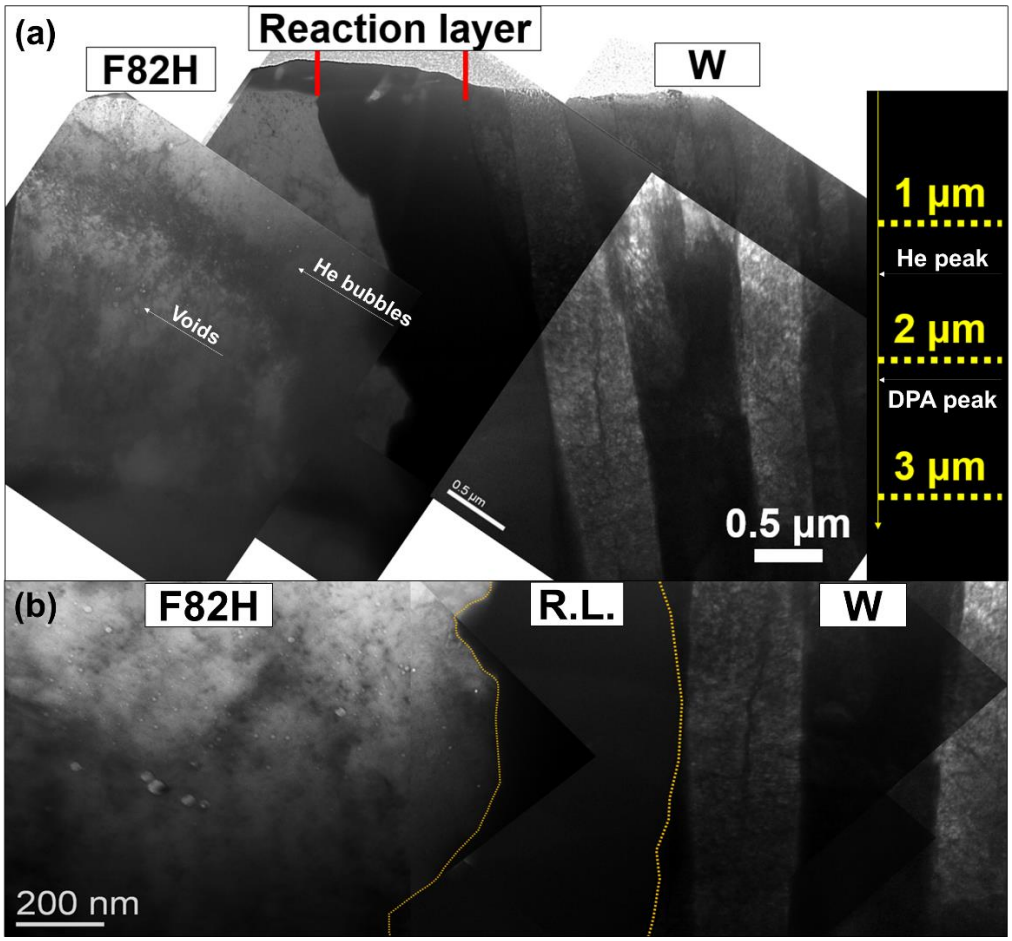

Figure 4.13 (a) In-focused microstructure of the F82H-20W composite after the ion-irradiation. (b) Under-focused TEM image over the depth range of 1000 nm to 1800 nm

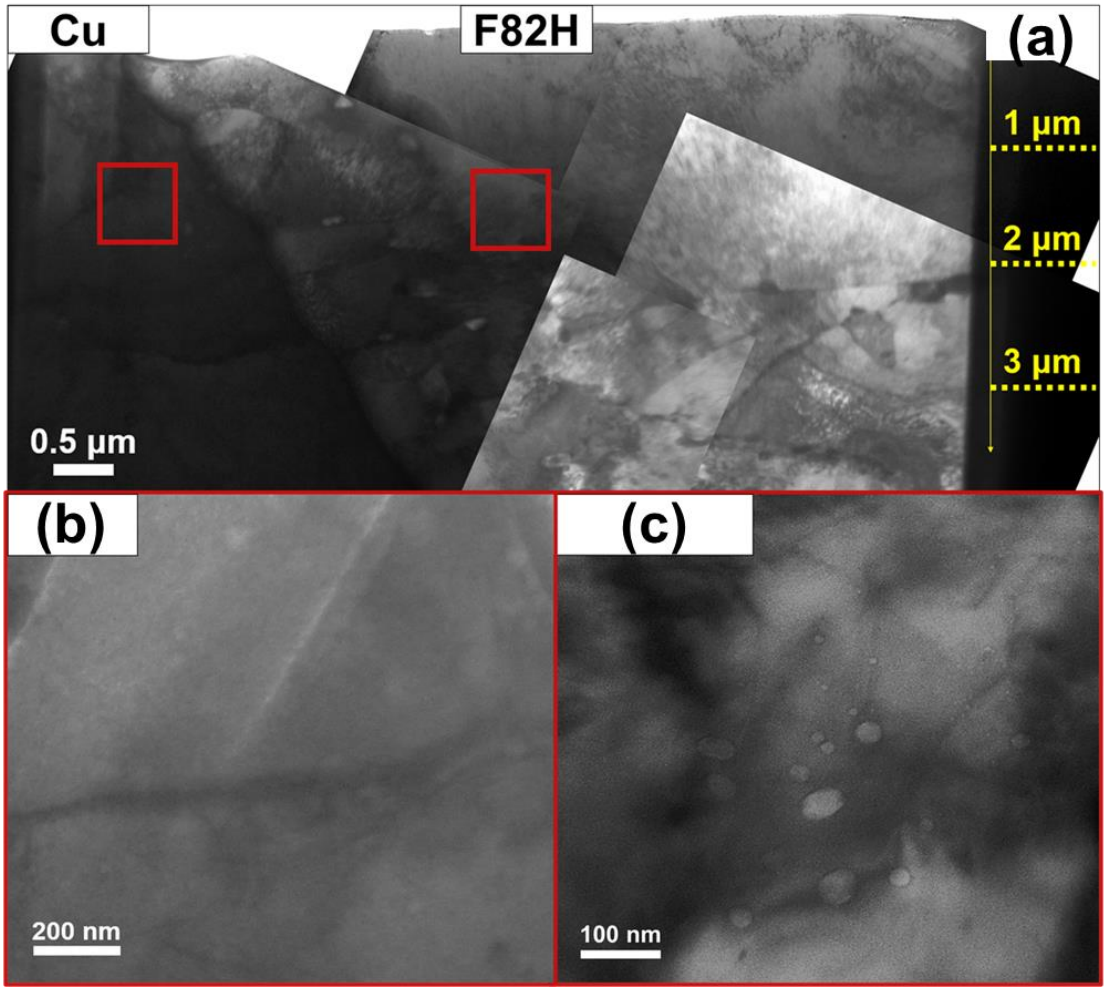

Figure 4.14 (a) In-focused microstructure of the F82H-20Cu composite after the ion-irradiation. (b) Cu part and (c) F82H part in F82H-20Cu composite of under-focused TEM image over the depth range of 1000 nm to 1800 nm

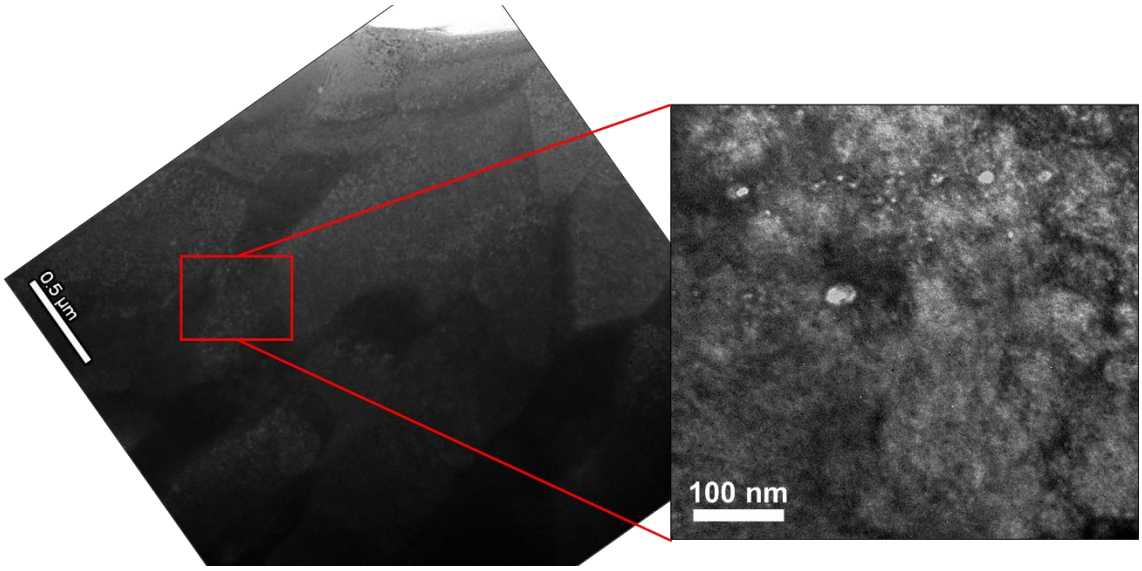

Figure 4.15 In-focused microstructure of the F82H-W reaction layer after the ion-irradiation and Under-focused TEM image over the depth range of 1100 nm to 1600 nm

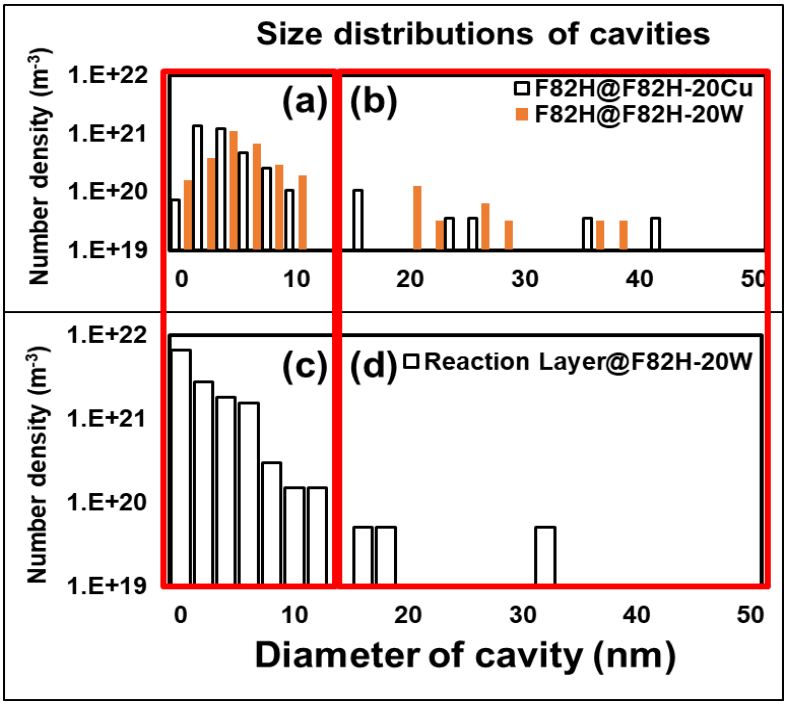

Figure 4.16 Size distributions of irradiation-induced cavities at (a)-(b) F82H areas in F82H-W and F82H-Cu composite materials and (c)-(d) the F82H-W reaction layer

Material	Number density of cavity (m^{-3})	Cavity diameter (RMC)	swelling (%)
F82H@F82H-20W	3.45×10^{21}	12.2 nm	3.26 %
F82H@F82H -20Cu	3.7×10^{21}	11.3 nm	2.63 %
F82H-W Reaction layer	1.34×10^{22}	2.86 nm	1.32 %

Table 4.6 The number density and diameter of root mean cube of cavities formed in F82H-based composite materials irradiated at triple ion-beam conditions

References

[1] TAN, Chao, et al. Investigation on 316L/W functionally graded materials fabricated by mechanical alloying and spark plasma sintering. Journal of Nuclear Materials, 2016, 469: 32-38.

[2] GREER, Julia R.; OLIVER, Warren C.; NIX, William D. Size dependence of mechanical properties of gold at the micron scale in the absence of strain gradients. Acta Materialia, 2005, 53.6: 1821-1830.

[3] NIX, William D.; GAO, Huajian. Indentation size effects in crystalline materials: a law for strain gradient plasticity. Journal of the Mechanics and Physics of Solids, 1998, 46.3: 411-425.

[4] SWADENER, J. G.; GEORGE, E. P.; PHARR, G. M. The correlation of the indentation size effect measured with indenters of various shapes. Journal of the Mechanics and Physics of Solids, 2002, 50.4: 681-694.

[5] JEON, Yong Jin; KIM, Se Hoon; DO KIM, Young. Effect of Fe7W6 phase (μ-phase) on mechanical properties of W-Ni-Fe heavy alloy. Journal of Korean Institute of Metals and Materials, 2011, 49.9: 720-725.

[6] MATĚJÍČEK, Jiří, et al. Tungsten-steel composites and FGMs produced by hot pressing. In: 21st International Conference on Metallurgy and Materials METAL. 2012.

[7] NOVAKOVA, A. A., et al. Low temperature formation of nanocrystalline Fe–W and Fe–Mo compounds. Journal of alloys and compounds, 2001, 317: 423-427.

[8] GUSTAFSON, Per. A thermodynamic evaluation of the C− Fe− W system. Metallurgical and Materials Transactions A, 1987, 18.2: 175-188.

[9] ZIEGLER, James F.; ZIEGLER, Matthias D.; BIERSACK, Jochen P. SRIM–The stopping and range of ions in matter (2010). Nuclear Instruments and Methods in Physics Research Section B: Beam Interactions with Materials and Atoms, 2010, 268.11-12: 1818-1823.

[10] ZIEGLER, James F. SRIM-2003. Nuclear instruments and methods in physics research section B: Beam interactions with materials and atoms, 2004, 219: 1027-1036.

[11] STOLLER, Roger E., et al. On the use of SRIM for computing radiation damage exposure. Nuclear instruments and methods in physics research section B: beam interactions with materials and atoms, 2013, 310: 75-80.

[12] SAHA, Uttiyoarnab; DEVAN, K.; GANESAN, S. A study to compute integrated dpa for neutron and ion irradiation environments using SRIM-2013. Journal of Nuclear Materials, 2018, 503: 30-41.

Chapter 5

Discussion

5.1 Differences of irradiation conditions between RAFM and F82H composite materials

For the reference RAFM steels, single Fe^{3+} or He^{+} ion beam was irradiated at 325 °C or room temperature. In order for the He implanted into the RAFM steels to aggregate to form bubbles, the annealing at 350 °C for 120 min was performed after He^{+} implantation. There was no formation of void in RAFM irradiated for only He ion. However, a large number of tiny He bubbles were observed. Radiation-induced dislocation loops were observed in RAFM and F82H after ion irradiation in the temperature range of 300 to 400 °C. As shown in figure 5.1, there was no observation of dislocation loop at the irradiation temperature of 500 °C. For F82H-based composite materials, triple fusion Fe^{3+}, H^{+} and He^{+} ion beam was irradiated at 350 °C and 500 °C. Comparing irradiation at 300 °C and 500 °C, average size and number density of voids decrease with increase of the irradiation temperature. As shown in figure 5.2, Wakai et al. reported that the swelling fraction decreased with the irradiation temperature under fusion triple beam irradiation condition at over 450 °C [9].

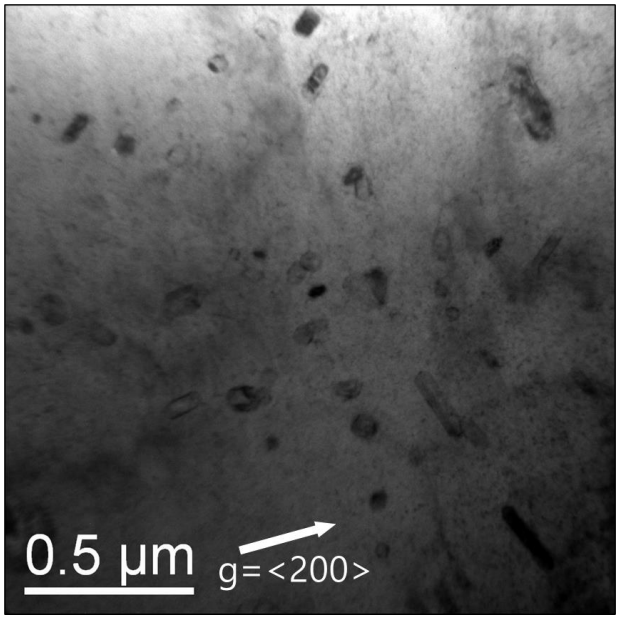

Figure 5.1 Microstructure of F82H irradiated for triple ion beam at 500 °C

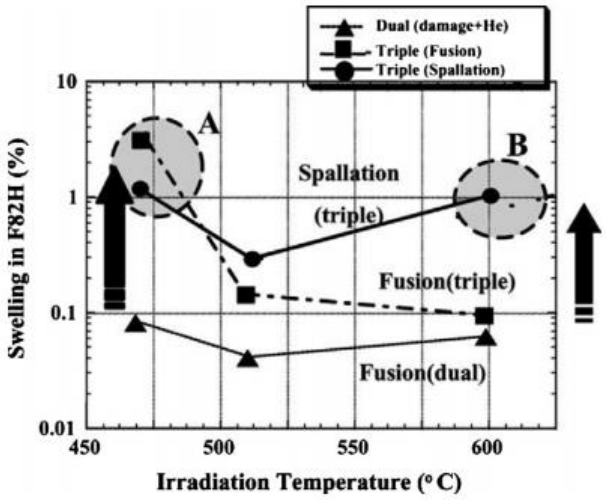

Figure 5.2 The dependence of swelling of F82H steels on irradiation temperature [9]

5.2 Irradiation Hardening

Since the ion irradiation sample has a shallow internal penetration depth of irradiated ions, it is essential to evaluate the mechanical properties at the nanoscale. The nano-indentation tests were performed to evaluate the ion-irradiation induced mechanical properties. In this chapter, for the F82H-20W and F82H-20Cu composite materials, the hardness changes according to the indenter contact depth was measured for a depth of 200 nm to 2000 nm by using Nano Indenter TI-950 (Hysitron) with a Berkovich tip which had been calibrated under the ISO-14577. The nano-indentation test was conducted to surfaces of F82H matrix, F82H-W reaction layer and W wire in the F82H-20W composite material and F82H matrix and Cu wire in the F82H-20Cu composite material at room temperature (R.T.). The nano-hardness measurements were carried out 15 times each at a specific depth for each material. In order to evaluate the irradiation hardening, the unirradiated area and irradiated area were tested. The depth profiles of the averaged nanoindentation hardness on the composite materials before and after the ion irradiation are presented in figure 5.3. As the contact depth of the indenter tip approaches the surface of the specimen, the indentation size effect (ISE) became larger. ISE is the observation during the nanoindentation test that hardness increases as the indent size decreases at nano-micro scales [3-4]. When the indent was created, the hardness of the material is not constant. At the small scale, materials would show higher hardness than at the macro-scale. The ISE has been seen through nano-indentation and micro-indentation measurements at varying depths. Dislocations increase the harness of measured material by increasing flow stress through dislocation blocking mechanisms.

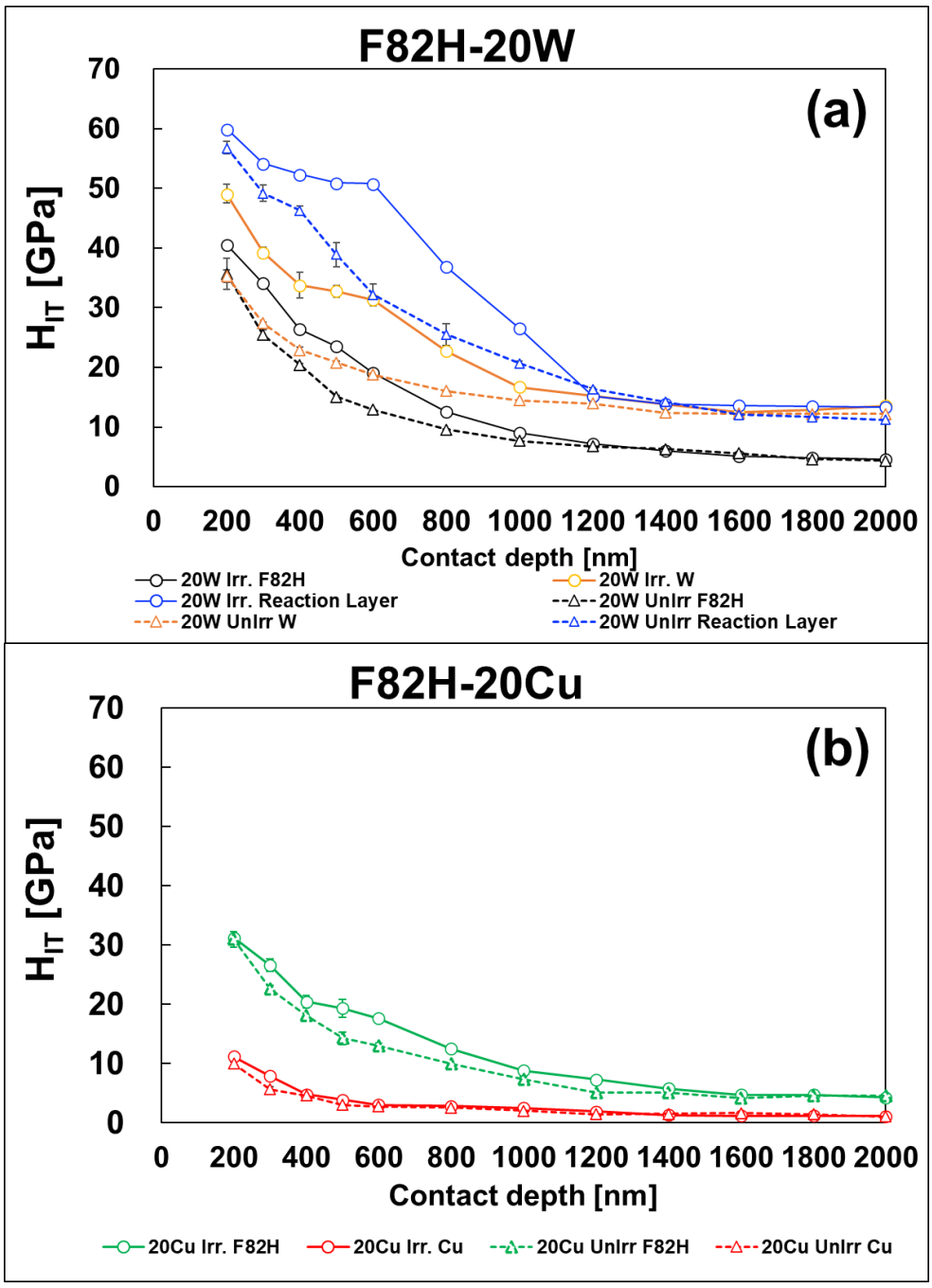

Figure 5.3 (a) The depth profiles of the averaged nanoindentation hardness on (a) F82H-20W and (b) F82H-20Cu before (△ mark) / after (○ mark) the ion irradiation

Even in the H-h graph for the composite materials measured in this chapter, the ISE in which the hardness value increases as the indentation depth decreases below a depth of 1000 nm occurs, making the analysis difficult. It shows the indentation size effect (ISE) for the composite materials irradiated as the condition following Fig. 5.3 for quasistatic indentations ranging in depth from 200 to 2000 nm.

Nix and Gao clearly explained the indentation size effect by considering the density of geometrically necessary dislocations generated by the indenter tip. All indentation hardness values interpolated from the curves in figure 3 for each contact depth are presented in Fig 4. The data in figure 5.4 was converted to Nix-Gao plot (H^2 vs 1/h). There were bilinear relationships with points of inflection over the depth range of 200 nm to 1000 nm, which was analyzed with a Nix-Gao plot using the formula expressed as:

$$H^2 = {H_0}^2 + {H_0}^2 \cdot \frac{h^*}{h}$$

with H as macroscale hardness value, H_0 as depth-independent hardness, h* as the material characteristic length scale and h as the indentation depth. The measurements at various contact depths confirmed the expected ISE upon hardness for all specimens. The ISE is assumed to be similar in both irradiated and unirradiated conditions. With F82H-20W composite material, the increased hardness of the irradiated material could be seen until shallow contact depth up to 1000 nm, compared to the nano-hardness of the unirradiated area as shown in Fig. 5.4 (a). In contrast, for F82H-20Cu composite material, the increase in hardness of the irradiated material is smaller than that of F82H-20W. And the contribution arising from the unirradiated substrate is negligible for depth from 1400 nm. The depth-independent hardness of the composite material was listed in Table 5.1.

Specimen	Contact material	Irradiated H0 (GPa)	Unirradiated H0 (GPa)	ΔH0 (GPa)
F82H-20W	Reaction layer	14.85	11.81	3.04
	W	7.81	3.51	4.30
	F82H	3.42	3.01	0.40
F82H-20Cu	Cu	1.06	0.98	0.08
	F82H	3.26	2.66	0.60

Table 5.1 H_0 and irradiation induced hardness changes of F82H-20W and F82H-20Cu composite material

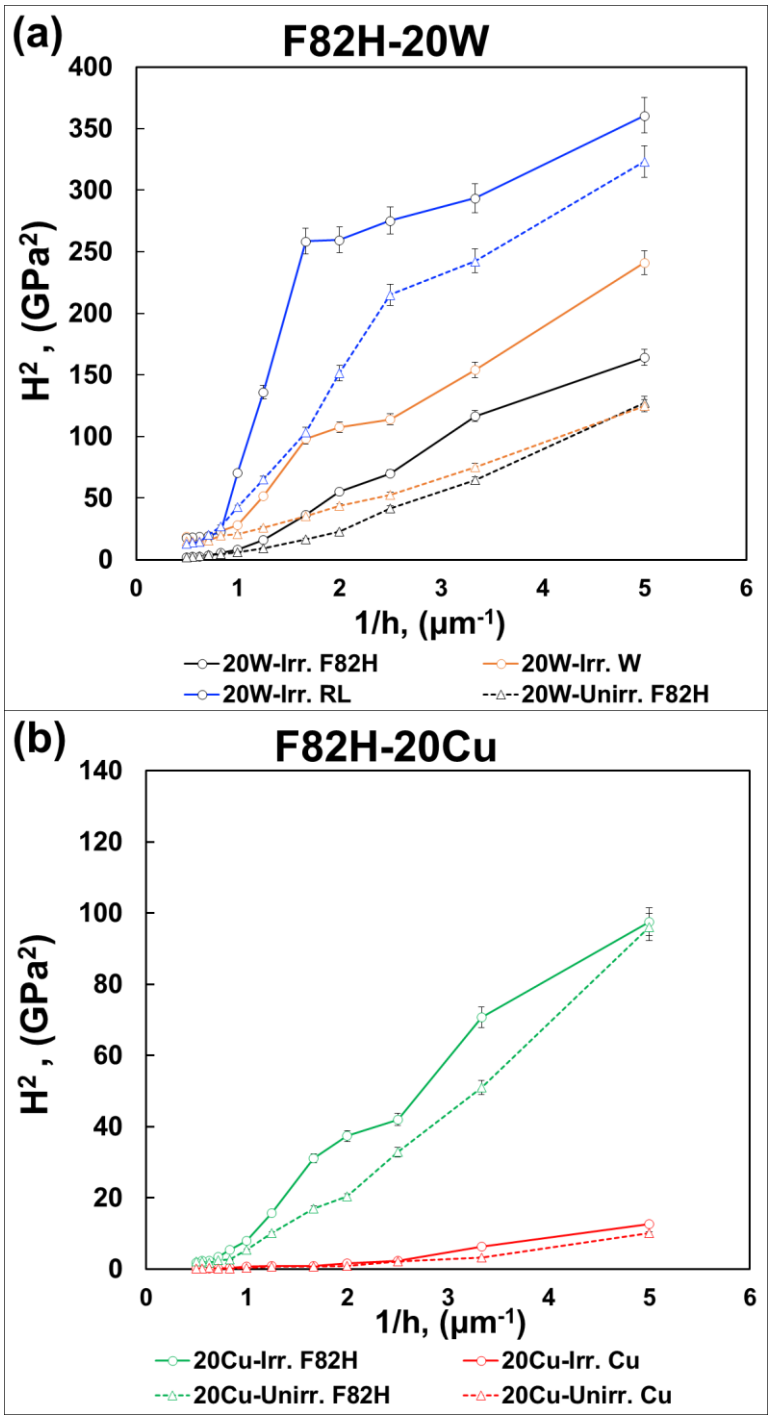

Figure 5.4 Nix-Gao plot for (△ mark) unirradiated and (△ mark) ion-irradiated (a) F82H-20W and (b) F82H-20Cu

Irradiation hardening was notable at the F82H-W reaction layer part in the F82H-20W

composite material. Owing to the reaction between Fe contained in F82H and W, there was a formation of Fe_7W_6 μ-phase intermetallic compounds (IMC). The Fe-W atomic bond of Fe_7W_6 μ-phase IMC shows brittleness and the feature of being easily broken, as well as a covalent characteristic. In the Nix-Gao plot for the brittle materials, such as the reaction layer with the Fe_7W_6 μ-phase IMC or tungsten, the change in slope could occur even in the unirradiated region. At shallow contact depth (<500 nm), many studies had reported Nix-Gao model overestimates the hardness values on various materials [1-6]. There were several inflection points at 300 nm to 500 nm depth in F82H-W reaction layer and W at the unirradiated conditions. As shown in Fig. 5.5, the Nix–Gao model overestimates the hardness values of several hard materials at such small depths [10]. Thus, the data should be analyzed in Nix-Gao model assuming that the dislocation spacing in the deformed volume is not uniform. Even considering the overestimation of hardness for unirradiated samples of hard materials, irradiation hardening is prominent in the F82H-W reaction layer and W of the F82H-20W composite material. In the F82H-20Cu composite material, less irradiation hardening occurred under the irradiation condition at 500 °C.

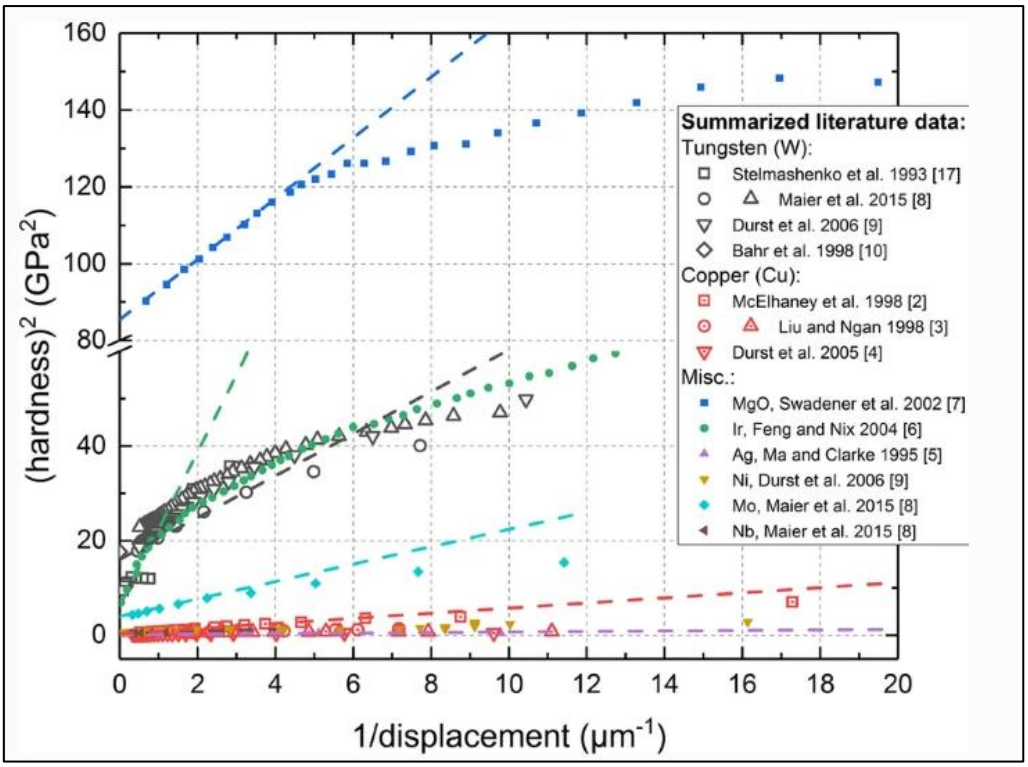

Figure 5.5 Overestimation of the value of nano-hardness in various unirradiated materials [10]

5.3 Thermal simulation

As shown in figure 5.6, the temperature distributions of various materials were presented. The upper side, which is contacted with the first wall, was set the temperature to 500 °C. At the bottom, there are two cylindrical cooling pipes with temperatures of 300 °C. In Fig. 5.6 (b), the average pore size was set to 500 μm of diameters. Total volume fraction of pores is 1% of the whole F82H. When 20 vol.% of wire is located inside F82H, faster heat transfer is possible. In addition, since heat exchange between the cooling pipe and the first-wall interface at the top can occur quickly by adding W or Cu wires, it can be seen that the F82H-W and F82H-Cu composites can decrease the average temperature inside the material.

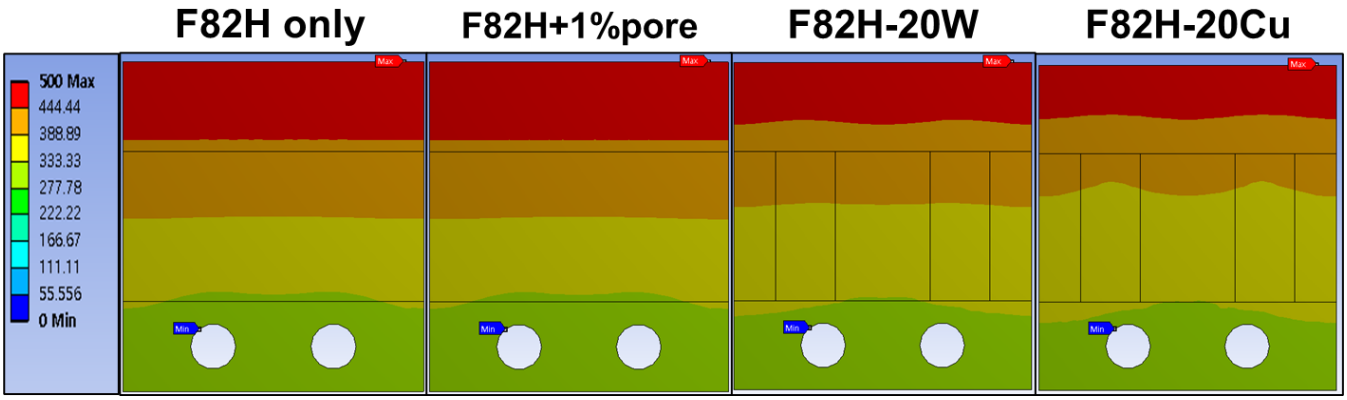

Figure 5.6 Temperature distribution in (a) F82H, (b) F82H including 1 vol.% pores, (c) F82H-20W and (d) F82H-20Cu

As listed in Table 5.2, when 20 vol.% of tungsten or copper is added, the temperature inside the material decreases by 2 °C and 5 °C on average, respectively. When 1 vol.% of pores are present inside F82H, the internal average temperature rises by 4.6 °C. Thus, in manufacturing a F82H-based composite material by adding wires, it is essential to minimize

the generation of pores that may occur during sintering of the F82H powder.

Sample	Average temperature, °C
F82H	382.6
F82H with 1 vol.% pore	387.2
F82H with 20 vol.% W wire	380.6
F82H with 20 vol.% Cu wire	377.6

Table 5.2 Simulated average temperature of composite materials

5.3 Summary

In this chapter, the microstructure and irradiation hardening effect were analyzed for the F82H-20W and F82H-20Cu composite materials irradiated with triple ion beam at a temperature of 500 °C. The microstructure observation showed that irradiation-induced He bubbles and voids were formed at F82H part in both composite materials, and the F82H-W reaction layer part in the F82H-20W composite material. In the reaction layer, a larger amount of He bubbles were formed than in F82H, but swelling fraction was smaller due to the overall size of He bubbles.

Irradiation-induced hardness change is assumed to be mainly due to the irradiation hardening in the F82H-W reaction layer and W and additionally to cavities in F82H. Irradiation-induced increases in nano-hardness were observed for each material on F82H-20W and F82H-20Cu composite materials. Triple ion-beam irradiation at the temperature of 500 °C gives rise to more irradiation hardening for F82H-20W composite material than F82H-20Cu composite material. In contrast, F82H-20Cu composite material shows less irradiation hardening. Adding Cu in an F82H-based composite material tends to decrease the irradiation hardening with the irradiation condition at the temperature of 500 °C.

Through the thermal simulation results, it could be confirmed that the use of tungsten or copper wires as an additive in the F82H-based composite material can quickly transfer the heat load from the first wall to the cooling tube. And it is important to find the suitable condition which can fabricate the composite material so that pores do not exist inside F82H or at the interface between F82H and additives.

References

[1] STANDARD, A. S. T. M., et al. Standard Practice for Characterizing Neutron Exposure in Iron and Low Alloy Steels in Terms of Displacements Per Atom (dpa). 2001.

[2] HAUŠILD, Petr. On the breakdown of the Nix-Gao model for indentation size effect. Philosophical Magazine, 2021, 101.4: 420-434.

[3] LIU, Wenbin, et al. Model of nanoindentation size effect incorporating the role of elastic deformation. Journal of the Mechanics and Physics of Solids, 2019, 126: 245-255.

[4] JANG, Jae-il, et al. Indentation size effect in bulk metallic glass. Scripta materialia, 2011, 64.8: 753-756.

[5] PHARR, George M.; HERBERT, Erik G.; GAO, Yanfei. The indentation size effect: a critical examination of experimental observations and mechanistic interpretations. Annual Review of Materials Research, 2010, 40: 271-292.

[6] PHARR, George M.; HERBERT, Erik G.; GAO, Yanfei. The indentation size effect: a critical examination of experimental observations and mechanistic interpretations. Annual Review of Materials Research, 2010, 40: 271-292.

[7] HEO, Jungwoo, et al. Ion-irradiation hardening of Ti/Ta-added reduced activation ferritic-martensitic steel evaluated with a new nanopillar fabrication technique. Journal of Nuclear Materials, 2018, 512: 184-192.

[8] BRIMBAL, Daniel, et al. Microstructural characterization of Eurofer-97 and Eurofer-ODS steels before and after multi-beam ion irradiations at JANNUS Saclay facility. Journal of Nuclear Materials, 2015, 465: 236-244.

[9] WAKAI, E., et al. Swelling behavior of F82H steel irradiated by triple/dual ion beams. Journal of nuclear materials, 2003, 318: 267-273.

[10] WANG, Jin, et al. The indentation size effect of single-crystalline tungsten revisited. Journal of Materials Research, 2021, 1-10.

Chapter 6 – Conclusion

F82H steel, one of the reduced activation ferritic-martensitic (RAFM) steel, is a strong candidate for the plasma-facing components (PFCs) in demonstration fusion plants (DEMO) type nuclear fusion reactor. Advantages of F82H steel include low coefficient of thermal expansion, stress corrosion cracking resistance, progenitor swelling resistance and dimensional stability after irradiation and He brittle resistance. On the other hand, in terms of low thermal conductivity, high temperature creep characteristics, irradiation brittleness, and welding problems, there are still research tasks to be supplemented. In order to improve the low thermal conductivity of the existing F82H, several composite materials with a higher thermal conductivity than that of F82H were prepared. And those thermal, mechanical and irradiation properties were measured and compared.

The basis experiments presented in the first half of Chapter 3 were performed on F82H-15W-5Cu, F82H-10W-10Cu and F82H-5W-15Cu composite materials. All composite materials in this chapter were manufactured through SPS at 850 °C for various holding time after adding wire to F82H powder to have a specific volume ratio. In the case of the composite material containing 5 vol.% of tungsten and 15 vol.% of copper, the increase in thermal conductivity was almost three times higher than that of the conventional F82H. However, all F82H-based composites showed very low mechanical properties. The major cause is that the inside of the F82H matrix was not completely sintered because it was manufactured at a relatively low temperature of 850 °C. In general, when the composite material has a relative density of 98% or less, it is judged that large pores exist inside. Thus, it was necessary to find the new SPS condition for densification of the composite materials. Nevertheless, the results on the increase of thermal conductivities indicate that W or Cu adding composite material would have the potential to be an F82H-based composite material

applicable to nuclear reactor components. In order to solve the above problem, SPS was performed at a temperature of 1000 °C. However, since copper with a low melting point of about 1085 °C is likely to be melted in SPS, in this experiment, the temperature increase rate from 100 °C/min was lowered to 50 °C/min. Moreover, when sintering for a long time at a temperature of 1000°C, normalizing occurs, and care should be taken that the microstructure of F82H is converted from martensite to ferrite. This concern was resolved by confirming that the internal microstructure of F82H part in the composite material sintered by holding at 1000°C for 2 hours had a Ferritic-Martensitic structure. As a result, F82H-20Cu composite material shows approximately 3.3 times higher thermal conductivity than general F82H. The increase in the amount of copper wire would be more effective in improving the thermal conductivity of F82H-based composite material compared with tungsten wire. Furthermore, due to no formation of reaction layer and tungsten carbide at the interface between wire and F82H matrix, F82H-20Cu showed a comparable tensile property compared to that of general F82H.

The microstructure and irradiation hardening effect were analyzed for the F82H-20W and F82H-20Cu composite materials irradiated with triple ion beam at a temperature of 500 °C. The microstructure observation showed that irradiation-induced He bubbles and voids were formed at F82H part in both composite materials, and the F82H-W reaction layer part in the F82H-20W composite material. In the reaction layer, a larger amount of He bubbles were formed than in F82H, but swelling fraction was smaller due to the overall size of He bubbles.

For the analysis of irradiation hardening, the triple ion-beam irradiation with 10.5 MeV Fe^{3+}, 1.05 MeV He^{+} and 0.38 MeV H^{+} was performed to well-polished surface of F82H-20W and F82H-20Cu composite materials. The irradiation induced increases in nano-hardness for F82H, W and F82H-W reaction layer in F82H-20W and F82H-20Cu composite materials.

However, there was no observation of irradiation hardening at Cu part in F82H-20Cu composite material. It is correlated with the irradiation temperature and the melting point of each material. The irradiation condition at the temperature of 500 °C is high for Cu to generate irradiation-induced defects such as dislocation loops, He bubbles or voids. In F82H, dislocation loops were not found similar to Cu, but cavities such as He bubbles and voids were found in the microstructure. In the F82H-W reaction layer, Fe_7W_6 μ-phase intermetallic compound, there were a huge amount of He bubbles, but a few voids inside. And, triple ion-beam irradiation at the temperature of 500 °C gave rise to more irradiation hardening for F82H-20W composite material than F82H-20Cu composite material. In contrast, there was no change of nano-hardness at Cu part in F82H-20Cu composite material.

Due to the above results, it could be assumed that F82H-20W composite material is not stable under the current irradiation conditions with a significant change in its intrinsic hardening characteristic. In contrast, insignificant differences of irradiation hardening inside each of the irradiated/unirradiated Cu in F82H-20Cu showed that irradiation hardening did not occur to Cu with the irradiation condition at the temperature of 500 °C. Owing to the irradiation temperature, which was close to the melting point of Cu, the post-irradiation defect yield of FCC-Cu remained almost constant up to a lattice temperature of 300 °C and showed a tendency to decrease sharply as the temperature increased.

The operating temperature range of RAFM steel to be applied as a structural material for a fusion reactor is about 350-550 °C. The RAFM steel was put a limit on the high and low temperature due to the deterioration of mechanical properties and irradiation-induced brittleness, respectively. In addition, with DEMO-type fusion reactors or commercial fusion reactors, a high neutron irradiation damage equivalent to about 150 DPA would be predicted until the end of the fusion reactor operation, thus the development of RAFM steel with improved resistance for irradiation brittleness is required. For the operation condition of a

nuclear fusion reactor at 500 °C, the critical embrittlement of F82H-W composite material may cause with the irradiation hardening on the F82H-W reaction layer. A high number density of cavities, less dislocation loops and swelling fraction were observed in F82H-W composites, while much less cavities observed in F82H-Cu composite irradiated at 500 °C. For these reasons, it is reasonable to be pursued more investigation on F82H-Cu composite materials to apply the composite to a fusion reactor.

Acknowledgments

Doctoral student’s life is harder than I thought. But it is more rewarding than my imagine. In particular, I believe that the past days of repeated research and discussion for a long time helped train me as a researcher who can do one's own part.

None of this would have been possible without LOAM members. I must start by thanking my supervisor, Hashimoto-sensei. From reading my early drafts to giving me many advice on the thesis to giving me help to live abroad, he was as important to my thesis getting done as I was. He also gave me solutions to many problems I encountered during my research and gave me the ability to think on my own. I will follow his sharp and insightful advice in order to improve my own scientific thinking. I sincerely hope I continue to have opportunities to interact with Hashimoto-sensei for the rest of my research career. I am indebted to Isobe-sensei. From the first time I met him in the interview before I entered the LOAM, he was friendly with me. Also, despite having a different research theme than mine, he gave me a lot of inventive advice and encouragement regarding the experiment. To Oka-sensei, you have really helped me with ion irradiation and TEM analysis. No matter how busy we were, you made time in every meeting to ask about my study. In particular, he presented me with many innovative ideas at an individual meeting, so I was able to write good content for my thesis.

To my lab-mates, thanks for the fun and support. To doctoral students, it was nice to be able to exchange opinions about research and experimental methods with the Ph.D. students. To post M2 and current M2 students, many thanks for help at the laboratory. Of all the people I have worked with in LOAM, I will easily miss hanging out with you the most. To Tatsuya, Zushi and Kamisawa, it was the greatest experience in my life. I really thanks to you. I was

able to study Japanese culture more deeply. I could learn Japanese easily with many beers and lemon-sawa at the Nomikai. To Eryo, your unassuming personality and valuable advice for me will remain a treasured memory. Above all, thank you for teaching me how to edit documents and write mail in Japanese. He has been extremely supportive of me throughout this entire process and has made sacrifices to help me get to this point. Ryota, it I cannot forget him who went through hard times together. To Mayuko, she cheered me on, and celebrated each accomplishment. Itaro was a source of great emotional support, and the best funny guy I knew in the lab.

To M1 students, you were the best kouhai in my life. You made me realize that I can learn something not only from my seniors but also from my juniors. We couldn't participate in local conferences or trips together under various adverse conditions, but thanks to you guys, I was able to live happily in LOAM. Although two years is neither short nor long, I believe that we are sharing enough memories and experiences.

To B4, I could see that the level of the B4 students increases as time goes by. It was really nice to see that you are doing your own research in just one year. I earnestly hope to have the chance to contribute to materials science and engineering field in the future through active collaborations with LOAMers.

And I would like to thank the members of my dissertation committee. To Miura-sensei, for kindly sharing his decades of wisdom in the mechanical property field. To Ohno-sensei, you offered a balancing perspective as an expert in microstructure control field. My presentation slides and thesis for the dissertation were enhanced with your help improving thesis materials and explaining skills.

Most of all, my family allowed me to initiate doctorate course. I’m very thankful to the sources that have supported me financially. I believe that a doctorate degree is not just a title given just because I have studied for a few more years, but rather a qualification that proves

me can make academic discussions with other researchers. All of this was possible because of my family. Although I am still lacking in learning, I will continue to study and develop so that I can lead others and become a person who can be appreciated by others.